

0 4 AUG 1998

REPORT DOCUMENTATION PAGE

Public reporting burden for this collection of information is estimated to average 1 hour per response, including gathering and maintaining the data needed, and completing and reviewing the collection of information. Send collection of information, including suggestions for reducing this burden, to Washington Headquarters Service, Davis Highway, Suite 1204, Arlington, VA 22202-4302, and to the Office of Management and Budget, Paperwork

AFRL-SR-BL-TR-98-

0592

1. AGENCY USE ONLY (Leave blank)		2. REPORT DATE Aug 3, 1998	3. REPORT Final Technical Report	15 Mar 95 to 14 Mar 98
4. TITLE AND SUBTITLE DAMAGE ACCUMULATION MECHANISMS IN THERMAL BARRIER COATINGS			6. FUNDING NUMBERS F49620-95-1-0201	
6. AUTHOR(S) Golam M. Newaz				
7. PERFORMING ORGANIZATION NAME(S) AND ADDRESS(ES) Mechanical Engineering Department WAYNE STATE UNIVERSITY 5050 Anthony Wayne Dr. Detroit, MI 48202 ; (313)577-3877; gnewaz@eng.wayne.edu			8. PERFORMING ORGANIZATION REPORT NUMBER	
9. SPONSORING/MONITORING AGENCY NAME(S) AND ADDRESS(ES) AFOSR/NA 110 Duncan Avenue, Ste B115 Bolling AFB, DC 20332-8050			10. SPONSORING/MONITORING AGENCY REPORT NUMBER F49620-95-1-0201	
11. SUPPLEMENTARY NOTES				
12a. DISTRIBUTION AVAILABILITY STATEMENT Approved for public release; distribution unlimited.			12b. DISTRIBUTION CODE	
13. ABSTRACT (Maximum 200 words) The primary focus of the investigation was to conduct a chronological evaluation of damage initiation and propagation in Electron Beam - Physical Vapor Deposition (EB-PVD) thermal barrier coated (partially stabilized zirconia) Rene N5 single crystal superalloy. Damage initiation and failure events due to thermal cycling were investigated. Early crack initiation was rationalized through interfacial asperity induced high stresses between the TBC and the PtAl bond coat. Analytical solution was forwarded for transient and steady-state residual stresses in the EB-PVD system. Oxide scale development as a function of time was predicted using Fick's Law. The deviation of experimental results from Fick's Law was attributed to microcrack interaction and coalescence. Oxide scale induced internal pressure on crack surfaces was shown to be a plausible mechanism for microcrack growth. Buckling analysis was used to estimate the critical size of delamination necessary (sixteen times the TBC thickness) for spallation. It was shown that for various thermal cycles, spallation life can be estimated based on critical oxide layer thickness. Thermal wave imaging technique was used to track damage condition as a function of thermal cycles. It was found that saturation of thermal wave amplitude corresponds to spallation life of the sample. This work provides a mechanism-based framework for life prediction in TBC systems.				
14. SUBJECT TERMS Thermal barrier coating (TBC), spallation, thermal cycling, residual stress, microcrack initiation, oxidation, Fick's Law, damage mechanisms, thermal wave imaging, life prediction			15. NUMBER OF PAGES 45	
17. SECURITY CLASSIFICATION OF REPORT Unclassified			16. PRICE CODE	
18. SECURITY CLASSIFICATION OF THIS PAGE Unclassified		19. SECURITY CLASSIFICATION OF ABSTRACT Unclassified		20. LIMITATION OF ABSTRACT UL

TABLE OF CONTENTS

	Page
INTRODUCTION	2
TRANSIENT RESIDUAL STRESSES	3
CRACK INITIATION DUE TO ASPERITY	4
INTERFACIAL CRACKS UNDER THERMAL LOADING	5
INTERFACIAL CRACKS UNDER THERMOMECHANICAL LOADING	6
DAMAGE ACCUMULATION MECHANISMS	7
EXPERIMENTAL ASPECTS	8
THERMAL CYCLING	8
THERMOMECHANICAL CYCLING	8
ANALYTICAL ASPECTS	8
RESULTS AND DISCUSSION	10
SUMMARY AND CONCLUSIONS	12
ACKNOWLEDGEMENT	13
REFERENCES	14
APPENDIX	37

19980903 012

INTRODUCTION

Thermal barrier coatings (TBCs) provide thermal insulation and the bond coat supports a high temperature gradient at the surface of high temperature alloy substrates. Application of these superalloy/TBC systems can be found in both aerospace and land-based gas turbine engines. In automotive applications, the piston head for diesel engine is coated to achieve longer life time and higher performance in terms of fuel reduction and power. However, these coatings have durability problems, due to the material and thermal mismatch between the coating and the metallic substrate. Thermal residual stresses develop during cool down from processing temperatures (Nusier, and Newaz, 1998; Chang, et al., 1987; Williamson, et al. 1993; Carapella et al., 1994; Evans et al., 1983). Environmental effects, specifically oxidation, and thermomechanical loading create additional stresses (Suo 1995; Mikata, and Taya, 1985; Kardomateas, 1989; Kardomateas, 1990; Kardomateas, and Chung, 1994).

These stresses may initiate microcracks such as debonding and radial cracks and can have profound effect on the response of the TBC and interfacial damage accumulation and failure (Nusier, and Newaz, 1998; Takeuchi and Kokini, 1994; Hornack and Kokini, 1988; Evans and Hutchinson, 1984; Bottega and Maewal, 1983; Yin, 1985; Chai, 1990; Ryan and McCafferty, 1995). Their understanding is essential to predict the behavior of the coatings and their performance.

Failure processes of TBCs have received considerable attention in the literature as engineers and designers have made efforts to improve the coating manufacturing process and properties to improve its performance in a variety of environments. Partially stabilized zirconia (YSZ) has been a popular TBC for numerous applications. The bond coat is often the oxidation barrier to the substrate. It may delay but can not prevent oxidation reaction. Oxidation of the underlying bond coat is common if component use temperature is high. Bond coat can be a number of material systems typically denoted as MCrAlY (M stands for a more oxidation resistant material such as Nickel) and PtAl. PtAl diffusion coating has been developed due to demands on coatings for gas turbine engines that must operate at significantly higher temperatures than required previously. PtAl is also cheaper in the long run process. The thermally grown oxide (TGO) layer is often alumina oxide, Al_2O_3 which grows between the TBC and the bond coat layers. Aluminum is consumed from the bond coat to form Al_2O_3 as oxygen diffusion takes place. The evolution of the damage process including oxidation within the TGO layer appears to control the overall spallation process. However, this progressive damage process have not been studied adequately. Rather, researchers have proposed a number of failure scenarios that lead to spallation. Because of inadequate information, either a physical or a phenomenological basis for relating spallation life to growth kinetics within the TGO layer or damage due to interlinking microcracks has not been possible. A number of fundamental issues remain unanswered. These include crack initiation, crack propagation, oxide growth, and total damage accumulation.

There are three most plausible scenarios that researchers have proposed to date to explain the spallation mechanism. Evans and coworkers (1983) proposed that due to cool down, planar compressive stresses within the TBC can lead to buckling provided there is interfacial delamination crack already present between the TBC and the substrate. They do not elaborate on how such a delamination crack may occur at the interface in the first place. Our recent calculations with the current EB-PVD TBC system show that the minimum delamination crack length required should be sixteen times the TBC thickness. Buckling of the TBC layer is

illustrated in Figure 1. We will term this failure model as Buckling Model. The growth of the delamination crack is possible due to local crack tip conditions which can experience both shear and out-of-plane tension. Another model for spallation is due to another author Evans (1989). The basic aspect of this model is that through-thickness shear crack is developed in the TBC layer under compressive conditions in the TBC as shown in Figure 2. This model can be termed as Through-Thickness Shear Model. Recently, Suo (1995) proposed the Wrinkle Model which was addressed earlier by a number of researchers as well (Siegler, 1993; Tolpygo and Grabke, 1994). According to this failure model, there is void formation under the TBC layer and folding effects may occur that lead to cracking of the TBC layer at various locations.

All of the analysis was done for a model case where the specimen was plasma-sprayed in air with a thin zirconia-yttria ($ZrO_2 - 8wt.\%Y_2O_3$) layer on a nickel-chromium-aluminum-zirconium bond coat. The properties of these layers are given in Table 1.

Characterize progressive damage evolution in EB-PVD TBC/superalloy systems leading to spallation and to develop mechanics-based models to rationalize the failure events are the main objectives for this investigation.

Firstly, the primary focus was set to analytically predict the transient thermal residual stress distribution at the various interfaces of the TBC/bond coat/superalloy system and compare the results with finite element stress analysis results. Evaluation of residual stresses is treated until it reaches a steady-state condition. These solutions provide an insight into the influence of thermal and material mismatch stresses at the interfaces in TBC coated superalloy systems, particularly, in identifying conditions that lead to interfacial separation due to thermal loads.

Secondly, the conditions for microcrack initiation due to thermal residual stresses at wavy interfaces and putting an empirical equation for these stresses were covered.

Thirdly, the evaluation of the conditions necessary for growth of different kinds of interfacial cracks under thermo-mechanical loading was covered.

Finally, the optical microscopy, scanning electron microscopy and thermal wave imaging techniques were used to characterize the interfacial damage of a two layer EB-PVD TBC on a single crystal superalloy (Rene' N5) substrate. Fick's law was used to describe the TGO buildup for early cycles.

TRANSIENT RESIDUAL STRESSES IN THERMAL BARRIER COATINGS: ANALYTICAL AND NUMERICAL RESULTS

Elasticity based modeling was used to determine the transient stresses in the TBC, the bond coat, and the superalloy substrate with specific attention to the interfaces. For the steady state case, finite element modeling was undertaken. Closed form elasticity solutions correlated well with the finite element results for the steady state case. The highest residual stresses occurred at the interface between the bond coat and the TBC. An important result of this investigation was that the TBC/bond coat interface was under biaxial stress field. An interesting result was that the residual stresses developed in the substrate are higher for the case of partly cooled specimen compared to the fully cooled specimen which can be rationalized due to the presence of higher temperature gradients at earlier times during cool down from processing temperature.

The orthogonal-expansion technique over a multilayer region was used in order to determine the temperature distribution in the concentric cylinders. The first three roots (ω_{jn}) were found to be dominant in prescribing the temperature field. All other roots are weak and were neglected. The axisymmetric condition was applied on the equilibrium equations along

with stress-strain relations and strain-displacement relations, so the equilibrium equations reduce to two ordinary differential equations. The transient stress field was obtained by applying the boundary conditions to the solution obtained from those ordinary differential equations. Transient residual stresses have been evaluated for the case of three concentric cylinder by finite element approach (steady state case only) as well as using elasticity approach. The analytical model is described in detail in the appendix as published in a refereed journal recently (Nusier, and Newaz, 1998).

Figure 1 shows the variation of radial stress versus radial distance at different time. The peak value occurred close to the center at $t=16.5$ second. Also Figure 1 shows that the radial stress vanish at the outer surface. Radial stresses are not critical for this specimen configuration because of their low values. Note that radial stress range is 0-25 MPa. Figure 2 shows the variation of tangential stress versus radial distance at different time, from this figure one can see that the maximum stress occurred in the bond coat. Figure 3 shows the variation of axial stress versus radial distance at different time, same as in Figure 2 the maximum axial stress occurred in the bond coat. These figures show excellent agreement between finite element solution and elasticity solution for the steady state case. The bond coat/TBC interface is clearly under biaxial stress field. The highest tensile stress is 242 MPa and the highest compressive stress is 132 MPa. The elasticity solution is not valid close to the free edge since the boundary conditions are not satisfied precisely at the free edge. The boundary conditions are subscribed in average form at any cross-section which may not be precisely valid at the free edge.

CRACK INITIATION IN THERMAL BARRIER COATINGS DUE TO INTERFACE ASPERITY

Microcracks have been observed to initiate near the bond coat/TGO interface after only a few thermal cycles in electron beam - physical vapor deposition (EB-PVD) TBC systems. The origin of these microcracks can be traced to the buildup of thermal stresses which may magnify due to asperity of the thermally grown oxide (TGO) layer and the bond coat. The TGO/bond coat interface was modeled as rough but periodic asperity. Finite element modeling was undertaken to determine the magnitude of stresses at a rough bond coat/oxide interface (modeled as a sine wave). Large normal interface stresses arise at the peaks of the rough interface, while large shear stresses arise at the mean line of the rough interface. It was found that these residual stresses can initiate microcracks at the bond coat/oxide interface that can result in debonding and can also develop cracks within the TGO layer. High wave amplitude and small wave length representing asperity create high normal and shear stresses at oxide peak and at the mean line of rough interface, respectively. In particular, the condition for microcrack initiation was investigated. The results show that asperity can result in stresses high enough to initiate microcracks at the TGO/bond coat interface.

The interface was modeled as a sine wave in the following form

$$S(r) = a_0 \sin\left(\frac{2\pi r}{\lambda}\right) \quad (1)$$

where $S(r)$ is the interface equation, a_0 is the wave amplitude, r is the radial coordinate, and λ is the wave length. The stresses of interest are the normal and shear stresses. Note that for the case of flat surface at the interface, the normal, and shear stresses are zero. On the other hand the tangential and hoop stresses are present, and they are very large in the oxide layer (4-5 GPa

compressive stress). Since the normal and shear interface stresses are acting directly on the interface, they should be continuous across the interface. Tangential and hoop stresses act within each layer on either side of the interface, and will therefore, be different in each material.

The uncoated superalloy specimen had a thickness of 3.175 mm, the bond coat layer thickness is 24.15 μm , the oxide layer thickness is 24.15 μm , the ceramic layer (TBC) thickness is 127 μm , and the radius of the specimen is 12.7 mm. The specimen was cooled down from a processing temperature of 1025 $^{\circ}\text{C}$ to room temperature of 25 $^{\circ}\text{C}$.

A parametric study was carried out in which the effect on interface stresses due to variation in three wave amplitudes, and four wave lengths representing different levels of asperity were considered. In this study the material properties were considered to be temperature dependent, so that the results will be more practical.

For the case of 2.413 μm wave amplitude and 31.75 μm wave length, the peak value of interface normal stress reaches a value of approximately 600 MPa which is too high compared to oxide tensile strength (≈ 215 MPa). For a radial length of about 10 μm , the interface normal stress is exceeding the tensile strength of the oxide layer, so a cracks of 10 μm will be created at the peaks of the rough interface. Since at the tips of these cracks, the normal stresses are still high, one can expect that these cracks will propagate to longer ones. On the other hand, the shear stress has a peak value at the mean line of the rough interface, for a case similar to the previous one, cracks of 15 μm or longer will be created at the mean line of the rough interface, since the tensile shear strength of the oxide/bond interface is approximately 70 MPa. Figures 4-5 show that the variation of normal stresses versus wave amplitude and the inverse of the wave length is close to be linear.

Based on the previous discussion the following empirical formulas seems to be a good fit for normal and shear stresses

$$\sigma_{nn} = \frac{2\pi a_0}{\lambda} \left(\frac{1+\nu_o}{2E_o} + \frac{1+\nu_b}{2E_b} \right)^{-1} \varepsilon \sin\left(\frac{2\pi r}{\lambda}\right) \quad (2)$$

$$\sigma_{nt} = \frac{2\pi a_0}{\lambda} \left(\frac{1+\nu_o}{2E_o} + \frac{1+\nu_b}{2E_b} \right)^{-1} \varepsilon \cos\left(\frac{2\pi r}{\lambda}\right)$$

where ε is the thermal strain, ν is Poisson's ratio, E is the modulus of elasticity, and subscripts o and b corresponding to oxide and bond coat layers, respectively. Figure 6 shows finite element results in comparison to the suggested empirical equations for normal stresses. Clearly the empirical equations are in good agreement with finite element results.

ANALYSIS OF INTERFACIAL CRACKS IN A TBC/SUPERALLOY SYSTEM UNDER THERMAL LOADING

Effect of interfacial microcracks have been investigated using fracture mechanics approach. In, particular, J-integral and the energy release rate G , for both Mode I and Mode II using virtual crack extension method were evaluated. Two types of specimens were studied. The specimens were cooled down from processing temperature of 1025 $^{\circ}\text{C}$ to 25 $^{\circ}\text{C}$. The variation of the properties as function of temperature were used for analysis. It was found that the use of temperature dependent properties in contrast to constant properties provide significantly different values of J-integral and G . For stepped-disc specimen with edge crack, crack growth is only due to Mode II, while for cylinder specimen with internal crack, crack growth is due to mixed-mode

loading. An important implication of this result is that edge delaminations in a disk specimen may only grow due to Mode II conditions under pure thermal loading. Shear fracture characteristics of interfacial cracks thus become important in the failure of the TBC.

The presence of circumferential crack between the ceramic layer and the bond coat layer was analyzed using finite element method. The general code ABAQUS was used for these analysis. The energy release rate G was estimated by using the virtual crack extension method.

Finite element method was used in order to determine the J-integral value and the energy release rate. Virtual crack extension method was used to evaluate the energy release rate for both Mode I and Mode II. For cylinder type specimen the uncoated Nickel based superalloy had a radius of 9.26 mm, the bond coat layer thickness is 0.184 mm, the TBC thickness is 0.556 mm, and the length of the specimen is 100 mm. For stepped-disk specimen, the disk radius is 40 mm, the bond coat layer thickness is 0.184 mm, the TBC thickness is 0.556 mm, and the uncoated Nickel based superalloy had a thickness of 9.26 mm.

Figure 7 shows the variation of J and G_I versus crack length ratio for cylindrical type specimen. Clearly both of them have a very close value, also J and G_I have a peak value higher than the steady state value at a smaller crack length. The critical value of the energy release rate for TBC is about $300\text{--}320 \text{ N.m/m}^2$ based on fracture toughness of pure ceramic material, so under applied thermal loading the crack length exceeds four times the TBC thickness, instantaneous crack growth leading to fracture may occur. The variation of J and G_{II} ($G_I = G_{II}$) versus crack length ratio for stepped-disk specimen is shown in figure 8. Both values are very close, and for a very short crack about the order of TBC thickness, the J and G_{II} has a significant value of about 140 N.m/m^2 . Note that for stepped-disk specimen under thermal loading, Mode I is essentially absent and primarily Mode II exists.

ANALYSIS OF INTERFACIAL CRACKS IN A TBC/SUPERALLOY SYSTEM UNDER THERMO-MECHANICAL LOADING

Effect of oxidation growth between bond coat and ceramic layer (TBC) can be modeled as volume increase. In this part of the investigation, we represent this change in volume as an induced pressure across the crack faces. Mixed-mode fracture analysis of a thin circular delamination in an-axisymmetrically multi layer circular plate is developed. Geometrical nonlinearity is included in the analysis, since we have a large deflection case. The elastic deformation problem of a circular plate subjected to a clamped boundary condition at the edge delamination, an out of plane pressure load, and a compressive stress due to thermal mismatch between different layers, was solved numerically using a Rayleigh-Ritz method. The strain energy release rate was evaluated by means of the path-independent J-integral. The numerical results of this problem based on the energy method were verified using finite element method. Both methods correlate well in predicting the energy release rate for Mode I and Mode II, deflection, and postbuckling solutions. The energy release rate G , for both Mode I and Mode II cases were evaluated using the virtual crack extension method. A four layer model which include the TGO layer was analyzed using finite element method, two cases were considered. Case one is a specimen with a crack at middle of the oxide layer (TGO) while case 2 is a specimen with an interface crack between bond coat and TGO layers. Also, for both cases, a sensitivity study for the effect of variation of materials properties ($\pm 25\%$) were undertaken using the finite element method.

The presence of circumferential crack between the ceramic layer and the bond coat layer

was analyzed using A Rayleigh-Ritz method and finite element method. The general code ABAQUS was used for finite element analysis. The energy release rate G was estimated by using the virtual crack extension method.

Finite element method was used in order to determine the J-integral value and the energy release rate. Virtual crack extension method was used to evaluate the energy release rate for both Mode I and Mode II crack growth. For stepped-disk specimen, the disk radius is 12.7 mm, the bond coat layer thickness is 0.04826 mm, the TBC thickness is 0.127 mm, and the uncoated Nickel based superalloy had a thickness of 3.175 mm. The specimen was cooled down from a processing temperature of 1025 °C to a temperature of 25 °C.

Figure 9 shows the variation of G_I and G_{II} versus pressure ratio for a delamination radius of twenty times the TBC thickness. This figure shows good agreement between finite element method results based on VCEM and numerical results. Mode I is dominant in this case. Figure 10 shows the variation of J-integral delamination radius from numerical analysis. From this figure one can obtain the conditions when the crack will propagate. From literature the critical energy release rate is varied between 100-300 N.m/m² for this system configuration. For a value of 300 J.m/m², and a delamination radius of four times the TBC thickness, the crack will propagate at induced pressure value equivalent to 500 atmosphere (\approx 50 MPa). This value is easy to develop due to volume increase because of oxide layer growth. Also, based on finite element analysis conducted by the authors for this system with a wavy interface, the results shows that an axial stress of 185 MPa can be developed for a sine wave interface with amplitude of 2.4 μ m and wave length of 127 μ m.

DAMAGE ACCUMULATION MECHANISMS IN THERMAL BARRIER COATINGS (EXPERIMENTAL AND ANALYTICAL EVALUATION)

Spallation is a major failure condition experienced by thermal barrier coatings (TBCs) subjected to thermal and mechanical loads. Although evidence of spallation is substantiated and mechanistic models to describe the failure condition is prevalent in literature, the progressive nature of damage evolution leading to spallation has not been addressed adequately. In this chapter, discussion on the investigation of damage evolution in partially stabilized zirconia TBC on Nickel-based single crystal superalloy, Rene N5. Thermal cycles were imposed on button and rod specimens with Electron Beam - Physical Vapor Deposition (EB-PVD) TBC coating. The bond coat was PtAl. Different thermal cycles profile were used for damage evaluation purpose. Progressive damage evolution was tracked using microscopy and thermal wave imaging technique on samples subjected to a series of thermal cycles. Fick's law was used to describe the thermally grown oxide (TGO) buildup for early cycles. It was found that Fick's law can be used to correlate between damage thickness and oxide thickness for different thermal cycles profile. The importance of this correlation is that, for a given thermal cycle profile and number of cycle, the oxide thickness can be found analytically using Fick's law, from this thickness one can determine the state of damage (damage thickness) by using the correlation formula. However, at higher number of thermal cycles, damage in the form of microcracks and their coalescence results in the loss of integrity of the TGO. Thus, both oxidation kinetics and damage appears to have significant roles to play as it relates to spallation. As these microcracks coalesce to form major delamination cracks or interlayer separation, the susceptibility for coating buckling is increased. The delamination cracks finally consume the TGO layer. The loss of TBC integrity from the bond coat and the substrate facilitates its buckling during cool down from elevated

temperature. Our estimations show that a delamination crack length of about twelve to sixteen times the TBC thickness is needed for the current material system to initiate buckling. Progressive microcrack linking is a possible mechanism to develop such critical delamination crack lengths. Physical evidence of buckling was found in specimens prior to complete spallation.

EXPERIMENTAL ASPECTS

A rapid temperature CM furnace (model 1610 BL (c)) was used for thermal cycling tests. A series of test according to table 2 was done to understand the damage accumulation mechanism in disk top type specimens. Each cycle has a heat up time of 9 min., a cooled down time of 10 min., and a T_{\min} of 200 °C. After each test, the specimen was potted, sectioned, grinded, polished, and microscopy pictures were taken, respectively. For some samples, thermal wave images were taken in to quantitatively identify the state of damage (location and size). Microscopy will provide some information on the damage state. Thermal and thermomechanical cycling tests on cylindrical type specimens were conducted by using the CM furnace and the hydraulic MTS machine with a heating control unit that was added, respectively.

THERMAL CYCLING

Thermal cycling tests on disk top and cylindrical type samples were conducted on a rapid temperature CM furnace (model 1610 BL (c)). The heating zone for this furnace is about 20 cm × 20 cm × 25 cm. To insure the uniformity of the temperature, four different thermocouples (Type K) were used, two of them located at the bottom of the furnace and they are very close to the samples. The other two thermocouples were located at the top of the furnace. A digital recorder (Honeywell) were used to record the temperature variation. It should be mentioned that, the four thermocouples were showing a temperature difference of about 3-4 °C at temperature of 1177 °C. A micristar controller was used to set the parameters used to define a thermal cycle, such as heat up time, hold time, cool down time, minimum temperature, and maximum temperature, etc.

THERMOMECHANICAL CYCLING

Thermomechanical cycling tests conducted on cylindrical type specimen were under taken, since this type of specimen is similar to turbine blades. The specimen will be under compressive load generated by a (55 Kip) hydraulic MTS machine fully controlled by a PC (P5-60) computer. Heating control unit was added to support the required temperature variation with time. The dimensions of cylindrical type specimen used are 5.9 mm in diameter and 60 mm in length.

ANALYTICAL ASPECTS (Growth of TGO Layer)

The development of the diffusion model and the associated governing equations is necessary to determine the time dependent oxide layer thickness. Diffusion is approached as the penetration of one substance, such as oxygen, into a porous solid matrix of a different substance.

$$\frac{\partial c}{\partial t} = (Dc_{,i})_{,i} \quad (3)$$

Eqn. 3 is Fick's second law, where D is defined as the diffusion coefficient ($\mu m^2 / s$), c is the oxygen concentration ($atom / \mu m^3$), and t denote time dependence. The temperature dependence is incorporated into the diffusion coefficient which is approximated by an Arrhenius type relationship

$$D = D_0 \exp\left(\frac{-Q}{RT}\right) \quad (4)$$

where D_0 is the diffusion constant ($\mu m^2 / s$), Q is the activation energy for oxygen diffusing into metallic substrate (J/mol), R is the universal gas constant ($8.134 J/mol K$) and T is the temperature (K). (6.16)

The oxidation growth law will be obtained from the experiments as function of D_p^{eff} and time, where D_p^{eff} is the effective oxidation constant and is defined as

$$D_p^{eff} = \frac{1}{t_c} \int_0^{t_c} D_0 \exp\left(\frac{-Q}{RT(t)}\right) dt \quad (5)$$

where $T(t)$ is the temperature which can vary with time.

The solution of the partial differential Eqn. 3 for a one dimensional problem is obtained by using separation of variables technique in the following form

$$c(x, t) = C_o - (C_i - C_o) \sum_{n=0}^{\infty} B_n \cos \lambda_n (x / L) e^{-\lambda_n^2 D / L^2} \quad (6)$$

where,

$$B_n = \frac{4 \sin \lambda_n}{2 \lambda_n + \sin 2 \lambda_n} \quad (7)$$

The eigenvalues λ_n are the roots for the following equation,

$$\lambda_n \tan \lambda_n - \alpha_s L / D = 0 \quad (8)$$

The constants used for analysis in this investigation were as follows (Wright, 1996):

Activation energy for oxygen diffusion: $Q = 321 \text{ kJ/mol}$

Diffusion constant: $D_0 = 3.85 \times 10^{-5} \text{ m}^2/\text{sec}$

Universal gas constant: $R = 8.314 \text{ J/mol K}$

The diffusion equation for along a cylinder, and for the case where the variation of concentration with the angle θ is zero (axisymmetric case) is given by

$$\frac{\partial c}{\partial t} = D \left(\frac{\partial^2 c}{\partial r^2} + \frac{1}{r} \frac{\partial c}{\partial r} \right) \quad (9)$$

The solution of the partial differential Eqn. 9 for a one dimensional problem is obtained by using separation of variables technique in the following form

$$c(x, t) = C_o - 2(C_i - C_o) \sum_{n=1}^{\infty} \frac{1}{\lambda_n J_1(\lambda_n)} J_0(\lambda_n r / R) e^{-\lambda_n^2 D / R^2} \quad (10)$$

where J_n is Bessel function of the first kind (order n). The eigenvalues λ_n are the roots for the following equation,

$$\lambda_n J_1(\lambda_n) - \frac{\alpha_s R}{D} J_0(\lambda_n) = 0 \quad (11)$$

Bond coat oxidation resistance has been clearly linked to increased durability of the TBC.

RESULTS AND DISCUSSION

OPTICAL MICROSCOPY / SCANNING ELECTRON MICROSCOPY (SEM)

The thermal cycle profiles used for conducting all tests for this research is shown in Figure 11. Specimens were tested for various thermal cycles and examined after the thermal exposures. Specimens were evaluated at different number of thermal cycles according to table 2. Complete spallation was observed in these specimens between 175-185 cycles (cycle A), 435-455 cycles (cycle B), and 100-205 cycles (cycle C). The thermally cycled samples were potted by using cold mounting epoxy resin. After curing for one day, the specimens were cut by using a Buheler Isomet 2000 diamond cutter. The samples were then ground and polished by using normal metallurgical procedures. The polished samples were observed under Olympus BX 60 optical microscope. A few samples were observed under a Hitachi 2000 Scanning Electron Microscope (SEM) at higher magnifications to observe the nature of delamination cracking within the TGO layer.

The formation of an oxide layer can be easily traced via microscopy at the interface between the TBC layer and the bond coat. Figure 12 shows the photomicrograph of a thermal barrier coated sample without any thermal cycling. As expected, no interfacial cracking and thermally grown oxide layer were evident at the bond coat/top coat (TBC) interface. Thermal cycling of samples in air leads to the formation of a reaction product layer and interfacial cracking/damage at the bond coat/top coat interface. This oxidation product (TGO) is Al_2O_3 and has been confirmed by many researchers. The TGO appears to grow thicker with higher number of thermal cycles. Also, within the TGO layer, numerous microcracks and void like discontinuities are formed. A few thermal cycles leads to the formation of interfacial cracking at the bond coat/top coat interface and with increasing the number of cycles leads to the formation of both interfacial cracking and TGO layer. Figure 13 show the photomicrographs of the interfacial cracking at the bond coat/top coat interface taken after 2 thermal cycles (cycle type A). Figures 14 through 17 show the chronological evaluation of interfacial damage in TBC due to thermal cycling at 25, 50, 110 and 175 (cycle type A). The thickness of the TGO layer grows with increasing the number of cycles.

After about 50 cycles (cycle type A), the TGO shows separation in the form of delamination. The separation between the TBC and the bond coat takes place through the TGO layer instead of delamination at any preferred interface. The separation width or damage width between the TBC and the bond coat continues to increase as number of cycles are increased. We

can address this cycle induced change by accounting for damage coalescence within the TGO layer and increased propensity for buckling of the TBC layer. We address this mechanism next.

Based on our analysis of top layer buckling on a circular plate, our estimates show that buckling is possible only if the delamination crack size is twelve to sixteen times or higher than the TBC thickness. The evidence of buckling in a specimen cycled to 175 (cycle type A) cycles where the separation width for delamination is considerably higher at the middle of the specimen than near the ends points out that the delamination crack through the TGO layer may reach such a critical length necessary to induce buckling. The evolution of damage in the form of microcracks and voids within this layer can interact to form such delamination cracks.

For only oxidation driven degradation, TGO layer growth can be described by Fick's law. The predicted TGO layer growth is shown in Figures 18 and 19 for cycle A & B respectively. The TGO layer growth in addition to separation thickness is termed in Figures 18 and 19 as "damage thickness". Damage thickness in this study is referred to any change in specimen structure, these changes can be oxide, separation, crack, voids, ...etc. Based on that when we have breakdown of the TGO layer, we refer to the difference between damage thickness and oxide thickness as separation. The experimental data which is an average of at least four optical micrographs for each point along the length of the TGO layer is shown in the same figure. A computer code (written in C++) was developed to evaluate the damage area from which the damage thickness can be evaluated. The input for this program is the output of a scanned optical micrograph in TIF format.

The deviation of experimental results from the predicted TGO layer thickness occurs at about 50 thermal cycles (cycle A) and at 130 thermal cycles (cycle B). According to Fick's law, these two cycles have approximately the same oxide thickness. The significance of this result is that below 50 thermal cycles of the type chosen in this investigation, the TGO layer growth is oxidation driven.

According to Eqn. 5, for any thermal cycle profile, an effective diffusion constant can be evaluated by numerical integration (Simpson's rule was used). After the effective diffusion constant has been determined, the oxidation thickness according to Eqn. 6 (button samples) and Eqn. 10 (cylindrical specimen) can be evaluated. A very interesting result were found, that is the damage thickness (experimental measurement) is equal to oxide thickness (Fick's law) up to a critical oxide thickness ($\approx 6.2 \mu\text{m}$), beyond that thickness, the damage thickness start to get bigger than the oxide thickness (separation thickness is the difference between damage thickness and oxide thickness), in another word separation start to occurred. At another critical oxide thickness ($\approx 13 \mu\text{m}$) the sample spall off. This observation has been proven for different thermal cycles profiles, different maximum temperature and different holding time were used (cycles type A, B, C and D). Figure 20 shows the variation in total damage thickness versus oxide thickness for four different thermal cycles. This figure clearly shows that four different thermal cycle profile follow same trend to failure. An important outcome from this figure, is that, for any thermal cycle profile and at any time during thermal exposure, the oxide thickness can be calculated very easy and straight forward by the use of Fick's law, knowing the oxide thickness will lead to identify the damage state (Figure 20). To develop Figure 20, the maximum temperature were varied between 1177-1132 °C (this is the recommended application temperature range for this kind of samples by GE), and the holding time were varied between 45-600 minutes. As will be discussed later on, the holding time has no effect on damage size as long as the sum of holding time is fixed. The maximum temperature has a major effect on life time, for example, reducing the maximum temperature from 1177 °C to 1135 °C will increase the

sample life time by a factor of 2.4. This observation is illustrated in Figure 21, this figure has been developed based on Fick's law and the critical oxide thickness to failure which is 13 μm . It is very clear that time to failure is highly dependent on the maximum temperature. A very important result that is obtained from this research is that, the oxide thickness evaluated by Fick's law can be still be used as a correlation parameter to define the state of damage for any thermal cycle profile and at any time during thermal exposure.

For the case of cylindrical type specimens, two specimens were run under 80 MPa compressive stress and thermal cycle type A. The first one failed at 103 cycle and the second sample failed at 112 cycle. Under the same conditions with zero compressive stress a third sample failed after 108 thermal cycle. The compressive stress shows no effect on life due to the fact that only a small part of the compressive stress was carried by the TBC (≈ 13 MPa). Based on these three samples and Fick's law (Eqn. 10), a critical oxide thickness to failure was determined as 10.5 μm .

Figure 22a shows the thermal wave image of four samples at 0, 25, 50 and 100 thermal cycling (cycle A) respectively from left to right. The corresponding surface temperature profile plots shown on the right hand side of the figure represents the relative amplitude plotted as function of position or distance across the center of the samples. The plot indicates that the thermal wave signal amplitude increases 100% from 0 thermal cycling to 25 thermal cycling, while the change in the thermal wave signal amplitude from 25 thermal cycling to 50 thermal cycling is only 10% for each case. Figure 22b shows the thermal wave image of a second set of samples at 0, 150, 175 thermal cycling, respectively, from left to right. The corresponding surface temperature profile shows that the thermal wave signal amplitude increases 150% from 0 thermal cycling to 150 thermal cycling, however, the thermal wave signal amplitudes of the 150 thermal cycling and 175 thermal cycling samples are identical. With greater number of thermal cycles, the damage thickness at the bond coat/top coat interface are also increased. The damage thickness may also change depending on the number of thermal cycles. This damage thickness may be responsible for the thermal wave signal amplitude to vary.

SUMMARY AND CONCLUSIONS

- Analysis of concentric cylinder model representing TBC/bond coat/superalloy system showed that elasticity solution and numerical results from finite element stress analyses (steady state case only) correlate well in predicting thermal residual stresses in the various layers and at the interfaces. The highest stresses were found to occur at the bond coat/TBC interface. At this interface, results indicate a biaxial stress field due to high axial and tangential stress; the radial stress component was relatively small. The residual stresses developed in the substrate are higher for the case of partly cooled specimen compared to the fully cooled specimen because the temperature field has a high gradient at earlier stages compared to later stages.
- Finite element modeling was undertaken to determine the variation in residual stresses at a rough bond coat/oxide interface (modeled as a sine wave). Large normal interface stresses arise at the peaks of the rough interface, while large shear stresses arise at the mean line of the rough interface. High wave amplitude and small wave length signifying different conditions of asperity create a high normal and shear stresses at oxide peak and at the mean line of rough interface, respectively. In particular, the condition for microcrack initiation was determined. The results show that asperity can result in stresses high enough to initiate microcracks. Suggested empirical equations for normal and shear stresses are in good agreement with finite element results.

- Effect of interfacial microcracks have been investigated using fracture mechanics approach under pure thermal loading. The use of temperature dependent properties in contrast to constant properties provide significantly different values of J-integral and G values. Edge delaminations in a stepped-disk specimen may only grow due to Mode II conditions under pure thermal loading. Cylindrical type specimen with a circumferential crack has mixed mode conditions under pure thermal loading. For a stepped-disk specimen with a very short edge crack, the energy release rate and J-integral values are significantly high. This is expected, because of the stress singularity at the bimaterial interface at the free surface.
- Effect of interfacial microcracks was investigated using fracture mechanics approach under thermo-mechanical loading. Thermal load was used in conjunction with internal surface induced pressure for interfacial cracks. Stepped-disk type specimen with a central crack has mixed mode conditions under thermo-mechanical loading. The maximum deflection and total energy release rate evaluated by the finite element method and the energy method are in very good agreement. For a TBC toughness value of 300 J.m/m^2 , and a delamination radius of four times the TBC thickness, the crack will propagate at induced pressure value equivalent to 500 atmosphere ($\approx 50 \text{ MPa}$). The results clearly indicate that small internal pressure due to oxidation induced volume change may create the necessary conditions for crack growth during thermal cycling. This value may easily develop due to volume increase because of oxide layer growth or due to the presence of a wavy interface.
- Progressive damage evolution was tracked using microscopy and thermal wave imaging technique on samples subjected to a series of thermal cycles. It was found that Fick's law can be used to correlate between damage thickness and oxide thickness for different thermal cycles profile. The maximum temperature has a major effect on lifetime, for example, reducing the maximum temperature from $1177 \text{ }^\circ\text{C}$ to $1135 \text{ }^\circ\text{C}$ will increase the sample lifetime by a factor of 2.4. If the sum of the holding times is kept constant, then it leads to similar damage state, that is, isothermal and thermal cycling have similar damage states provided that the peak temperature is the same.
- Based on the investigation undertaken in the study, initiation of microcracks at the TGO/Bond coat interface can be related to asperity induced high stresses. Coalescence of these microcracks can be related to their growth influenced by oxide growth which may produce crack-surface pressure under thermal cycling. Finally, the coalesced microcracks can form a major delamination crack at the TGO/Bond coat interface. For large delamination cracks (over 12 times TBC thickness), in-plane compressive stress in the TBC layer due to the cool-down part of the thermal cycle can lead to spallation of the TBC layer. Thus, the progressive nature of damage initiation and accumulation leading to TBC failure are forwarded in this study and are rationalized through mechanics analyses.

ACKNOWLEDGEMENT

The principal investigator gratefully acknowledges the support of AFOSR, specially, Dr. Ozden Ochoa – program monitor for encouragement during the course of the program. Samples for this program were supplied by GEAE. Mr. P. Kennard Wright of GEAE is thanked for his support and interaction.

REFERENCES

- Bottega, W. J., and Maewal, A., 1983," Delamination Buckling and Growth in Laminates", Transactions of the ASME, Vol. 50, 184-189.
- Bottega, W. J., and Maewal, A., 1983," Dynamics of Delamination Buckling", Int. J. Non-Linear Mechanics, Vol. 18, No. 6, 449-463.
- Carapella, E. E., Hyer, M. W., Griffin, O. H., and Maahs, H. G., (1994), "Micromechanics of Crenulated Fibers", J. of Comp. Mat., Vol. 28, No. 14 1322-1346.
- Chai, H., 1990," Three-Dimensional Fracture Analysis of Thin-Film Debonding", Int. J. Fracture, Vol. 46, 237-256.
- Evans, A. G., Crumley, G. B. and Demaray, R.E., 1983," On the Mechanical Behavior of Brittle Coatings and Layers," Oxidation of Metals, Vol. 20. Nos.5/6, pp. 193-214.
- Evans, A.G. and J. W. Hutchinson, 1984, On the Mechanics of Delamination and Spalling in Compressed Films, Int. J. Solids and Structures, Vol. 20, No. 5, pp. 455-466.
- Evans, H.E., 1989,"Cracking and Spalling of Protective Oxide Layers," J. of Materials Science and Engineering, A120, pp. 139-146.
- Kardomateas, G. A., 1989,"Transient Thermal Stresses in Cylindrically Orthotropic Composite Tubes", J. of App. Mechs. 56. 411-417.
- Kardomateas, G. A., 1990,"The Initial Phase of Transient Thermal Stresses due to General Boundary Thermal Loads in Orthotropic Hollow Cylinders", J. of App. Mechs., 57. 719-724
- Kardomateas, G. A., and Chung, C. B., 1994,"Boundary Layer Transient Hygroscopic Stresses in Orthotropic Thick Shells Under External Pressure", J. of App. Mechs., 61 161-168
- Kokini, K., and Hornack, T. R., 1988,"Transient Thermal Load Effects on Coatings Bonded to Cylindrical Substrates and Containing Circumferential Cracks", J. of Eng. Mat. and Tech., 110, 35-40
- Mikata, Y., and Taya, M. (1985),"Stress Field in a Coated Continuous Fiber Composite Subjected to Thermo-Mechanical Loadings", I. of Comp. Mat. 19 554-578.
- Nusier, S. Q., and Newaz, G. M., 1998,"Transient Residual Stresses in Thermal Barrier Coatings: Analytical & Numerical Results", J. of Applied Mechanics, Vol. 65, No. 2, 346-353.
- Newaz, G. M., Nusier, S. Q., and Chaudhury, Z. A., 1998,"Damage Accumulation Mechanisms in Thermal Barrier Coatings", ASME, J. Engineering Materials and Technology, Vol. 120, No. 2, 149-153.

Nusier, S. Q., and Newaz, G. M., 1996, "Analysis of Interfacial cracks in a TBC/Superalloy System under Thermal Loading", to appear in the J. of Engineering Fracture Mechanics.

Nusier, S. Q., and Newaz, G. M., 1997, "Analysis of Interfacial Cracks in a TBC/Superalloy System Under Thermo-Mechanical Loading", presented at the International Gas Turbine & Aerospace Congress & Exhibition, Orlando, Florida-June 2-June 5, 1997, accepted for publication in the Transactions of the ASME, J. of Gas Turbines & Power.

Ryan, R. L., and McCafferty, E., 1995, "Rupture of an Oxide Blister", J. Electrochem. Soc., Vol. 142, No. 8, 2594-2597.

Suo, Z., 1995, "Wrinkles of the Oxide Scale on an Aluminum-Containing Alloy at High Temperature", J. of Mechanics of Physics and solids, Vol. 43, No. 6, 829-846.

Takeuchi, Y. R., and Kokini, K., 1994, "Thermal Fracture of Multilayer Ceramic Thermal Barrier Coatings", J. of Eng. for Gas Turbs. and Power. Transactions of the ASME, 116, 266-271

Williamson, R. L., Rabin, B. H., and Drake, J. T. (1993), "Finite Element Analysis of Thermal Residual Stresses at Graded Ceramic-Metal Interfaces. Part I. Model description and geometrical effects", J. Appl. Phys. 74 1310-1320.

Wright, K.P., 1996, Private Communication, GE - Evendale, Ohio.

Yin, W., 1985, "Axisymmetric Buckling and Growth of a Circular Delamination in a Compressed Laminate", Int. J. Solids and Structures, Vol. 21, No. 5, 503-514.

TABLE 1
Material properties at 22, 566 and 1149 °C

Material	Young's modulus (GPa)	Poisson's ratio	Coefficient of thermal expansion ($^{\circ}\text{C}^{-1}$)	Coefficient of thermal conductivity (W/m/k)	Coefficient of thermal diffusivity (m^2/s)
Substrate	175.8	0.25	13.91×10^{-6}	7	2×10^{-6}
	150.4	0.2566	15.36×10^{-6}	13	3.4×10^{-6}
	94.1	0.3224	19.52×10^{-6}	22	2.64×10^{-6}
Bond coat	137.9	0.27	15.16×10^{-6}	25	8×10^{-6}
	121.4	0.27	15.37×10^{-6}	50	13.56×10^{-6}
	93.8	0.27	17.48×10^{-6}	65	15.52×10^{-6}
TBC	27.6	0.25	10.01×10^{-6}	1	5×10^{-7}
	6.9	0.25	11.01×10^{-6}	0.96	3.51×10^{-7}
	1.84	0.25	12.41×10^{-6}	1	3.43×10^{-7}
Oxide	386	.257	6×10^{-6}		
	349	.257	8×10^{-6}		
	311	.257	8.9×10^{-6}		

Table 2
Test matrix for disk top type specimens

N_s	N_c	$T_{min}, ^\circ C$	$T_{max}, ^\circ C$	H.T min	C.T min	Hd.T min	Spall off	Sect.	T.W.I
1	2	200	1177	9	10	45	No	Yes	Yes
2	18	200	1177	9	10	45	No	Yes	Yes
3	25	200	1177	9	10	45	No	Yes	Yes
4	42	200	1177	9	10	45	No	Yes	Yes
5	50	200	1177	9	10	45	No	Yes	Yes
6	75	200	1177	9	10	45	No	Yes	Yes
7	100	200	1177	9	10	45	No	Yes	Yes
8	110	200	1177	9	10	45	No	Yes	No
9	150	200	1177	9	10	45	No	Yes	Yes
10	175	200	1177	9	10	45	No	Yes	Yes
11	175	200	1177	9	10	45	Yes	No	No
12	185	200	1177	9	10	45	Yes	No	No
13	25	200	1132	9	10	45	No	Yes	No
14	50	200	1132	9	10	45	No	Yes	No
15	100	200	1132	9	10	45	No	Yes	No
16	150	200	1132	9	10	45	No	Yes	No
17	200	200	1132	9	10	45	No	Yes	No
18	250	200	1132	9	10	45	No	Yes	No
19	300	200	1132	9	10	45	No	Yes	No
20	390	200	1132	9	10	45	No	Yes	No
21	435	200	1132	9	10	45	Yes	No	No
22	455	200	1132	9	10	45	Yes	No	No
23	40	200	1172	9	10	60	No	Yes	No
24	100	200	1172	9	10	45	Yes	No	No
25	139	200	1172	9	10	45	No	Yes	No
26	205	200	1172	9	10	45	Yes	No	No
27	50	200	1172	9	10	60	No	Yes	Yes
28	50	200	1172	9	10	60	No	Yes	Yes
29	5	200	1172	9	10	600	No	Yes	Yes
30	5	200	1172	9	10	600	No	Yes	Yes

Where, N_s is sample number, N_c is cycle number, H.T is heat up time, C.T is cool down time, Hd.T is hold time, Sect. stand for wither the specimen has been sectioned or not, and T.W.I is the abbreviation for thermal wave imaging technique.

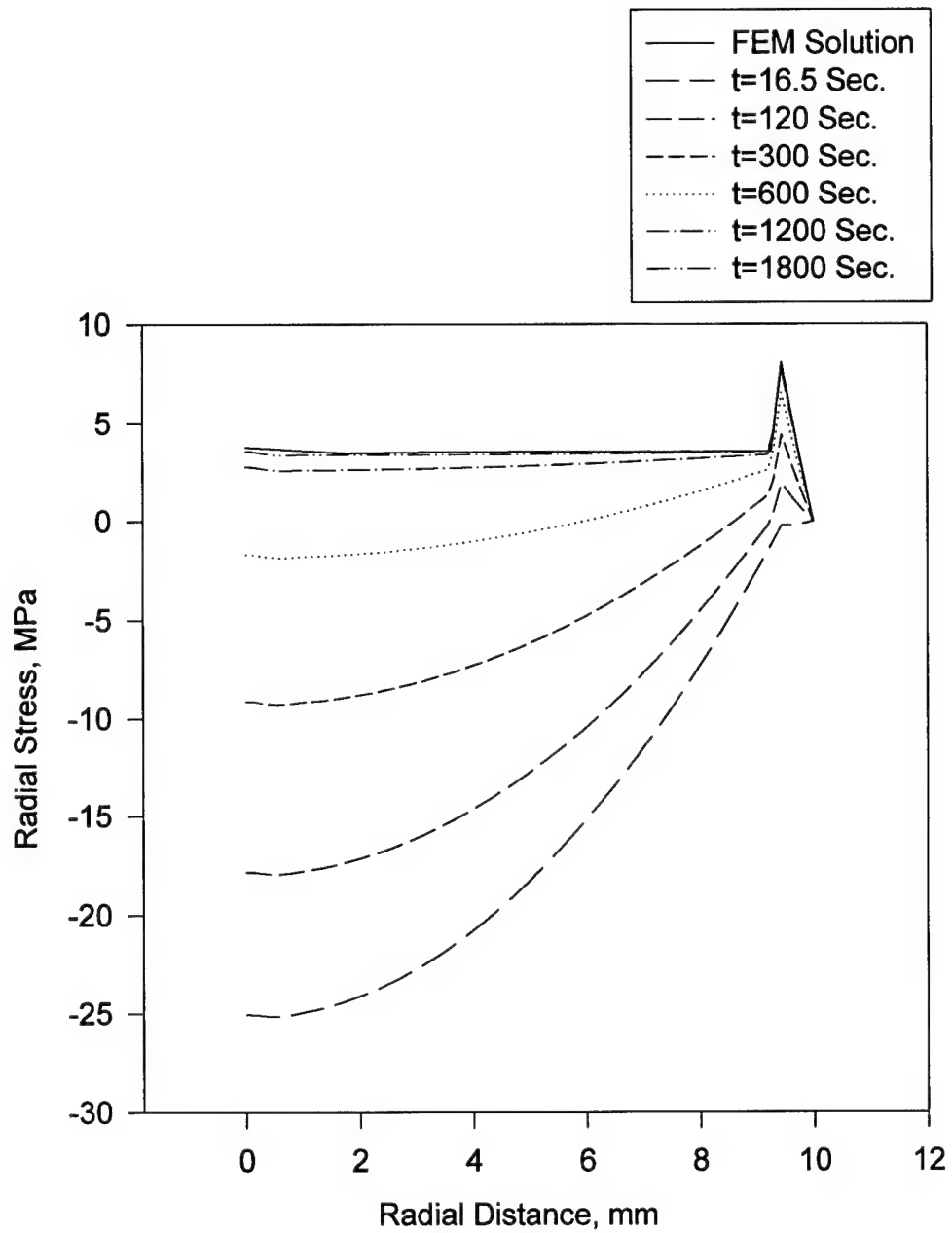


Figure 1. Radial stress versus radial distance at different time for the TBC/bond coat/superalloy system

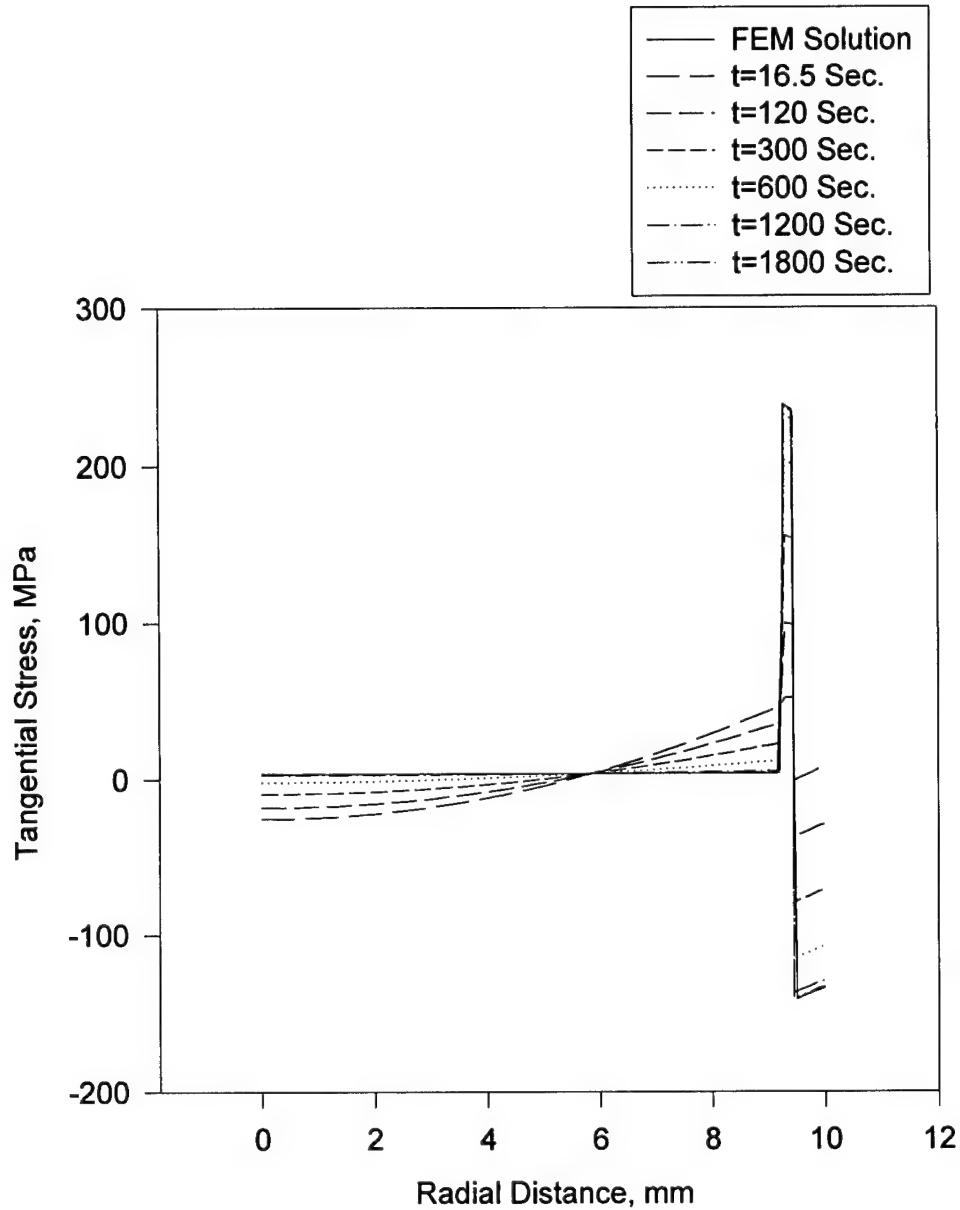


Figure 2. Tangential stress versus radial distance at different time for the TBC/bond coat/superalloy system

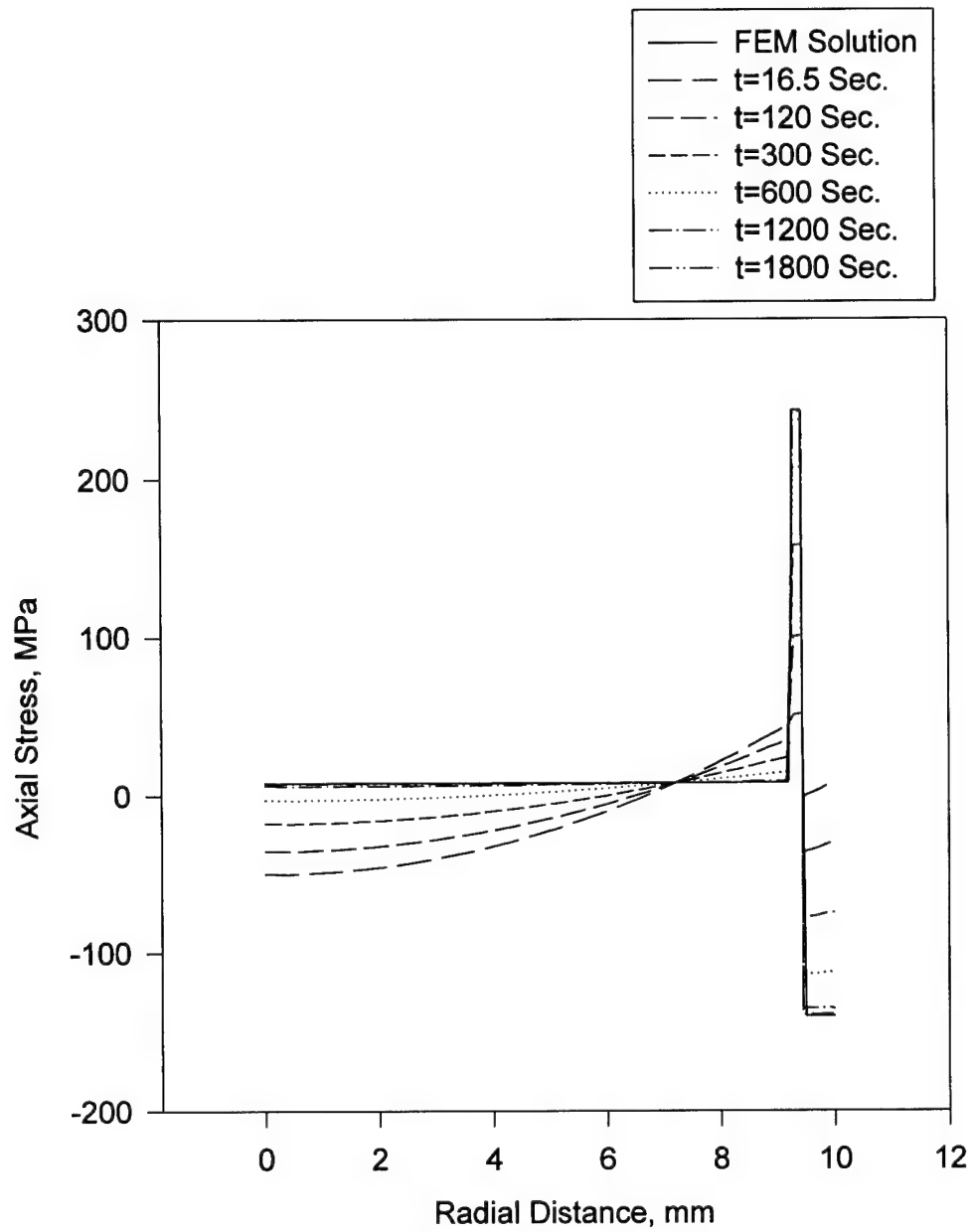


Figure 3. Axial stress versus radial distance at different time for the TBC/bond coat/superalloy system

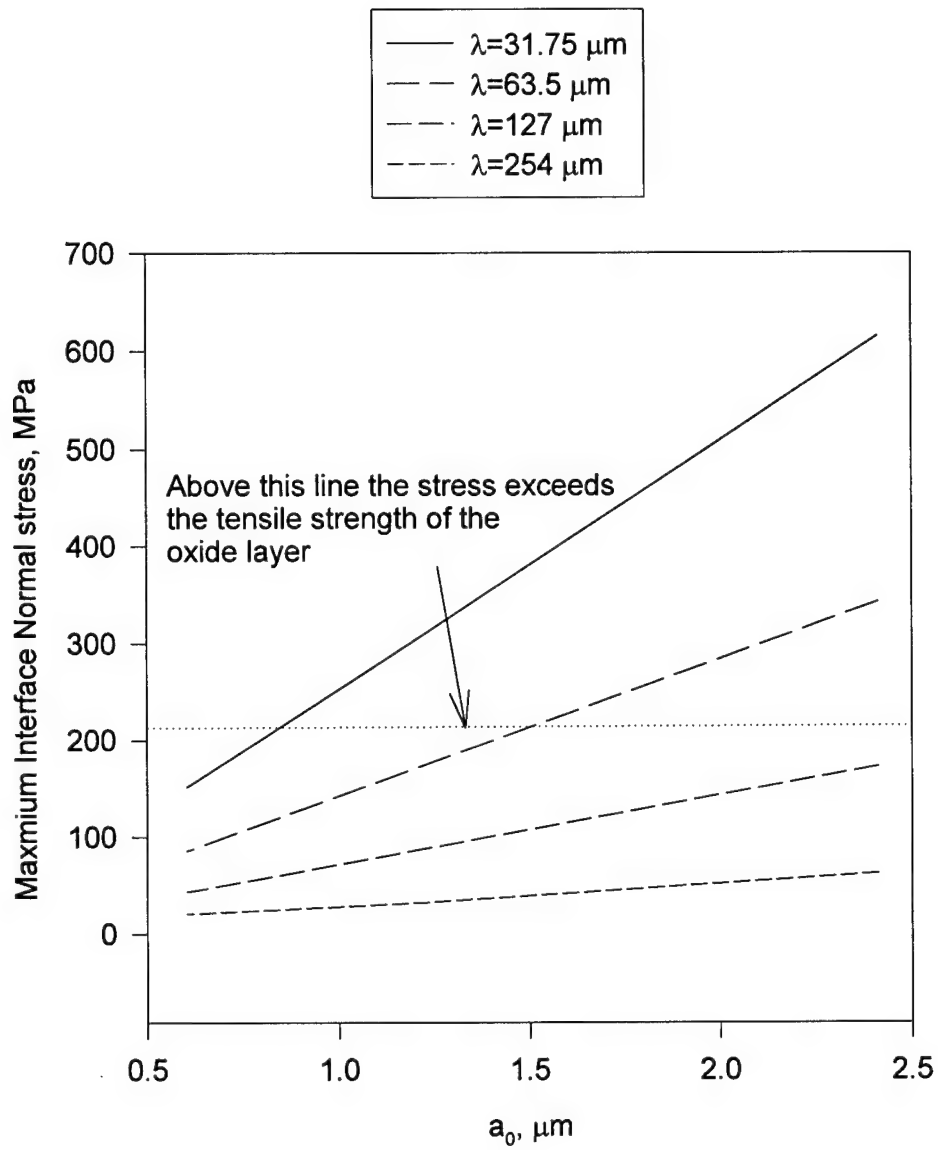


Figure 4. Maximum interface normal stress versus wave amplitude.

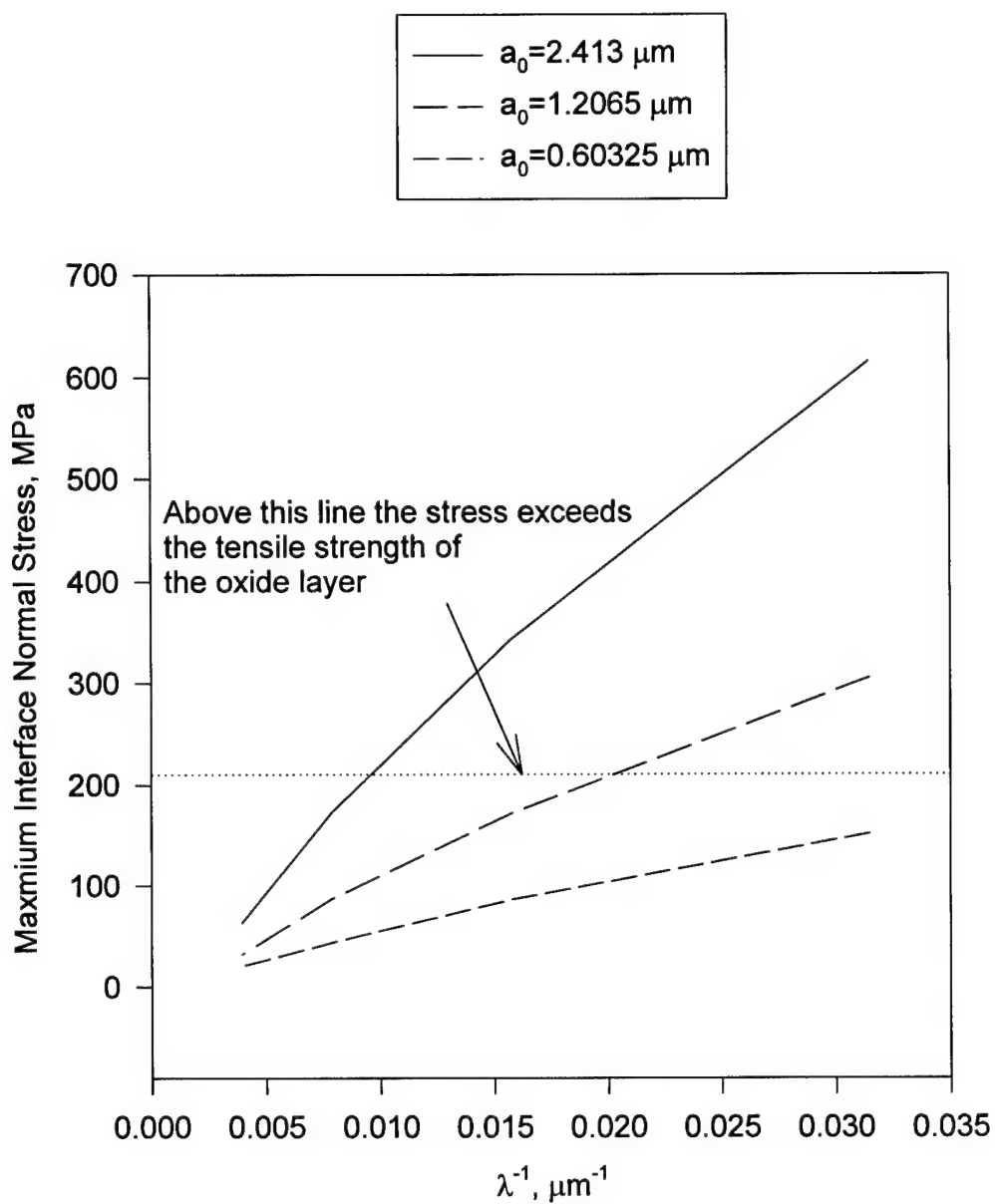


Figure 5. Maximum interface normal stress versus the inverse of the wave length.

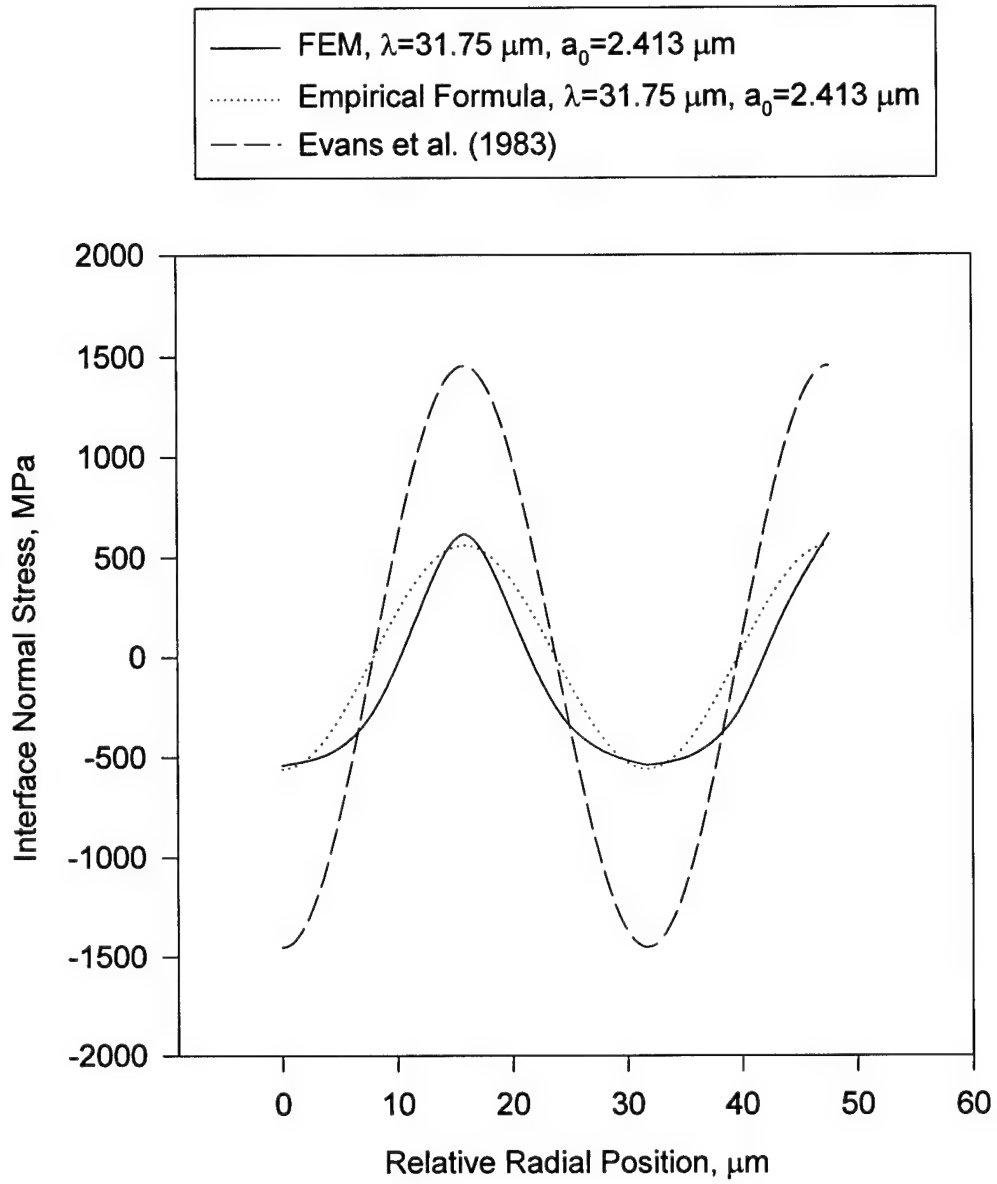


Figure 6. Interface normal stress versus radial position.

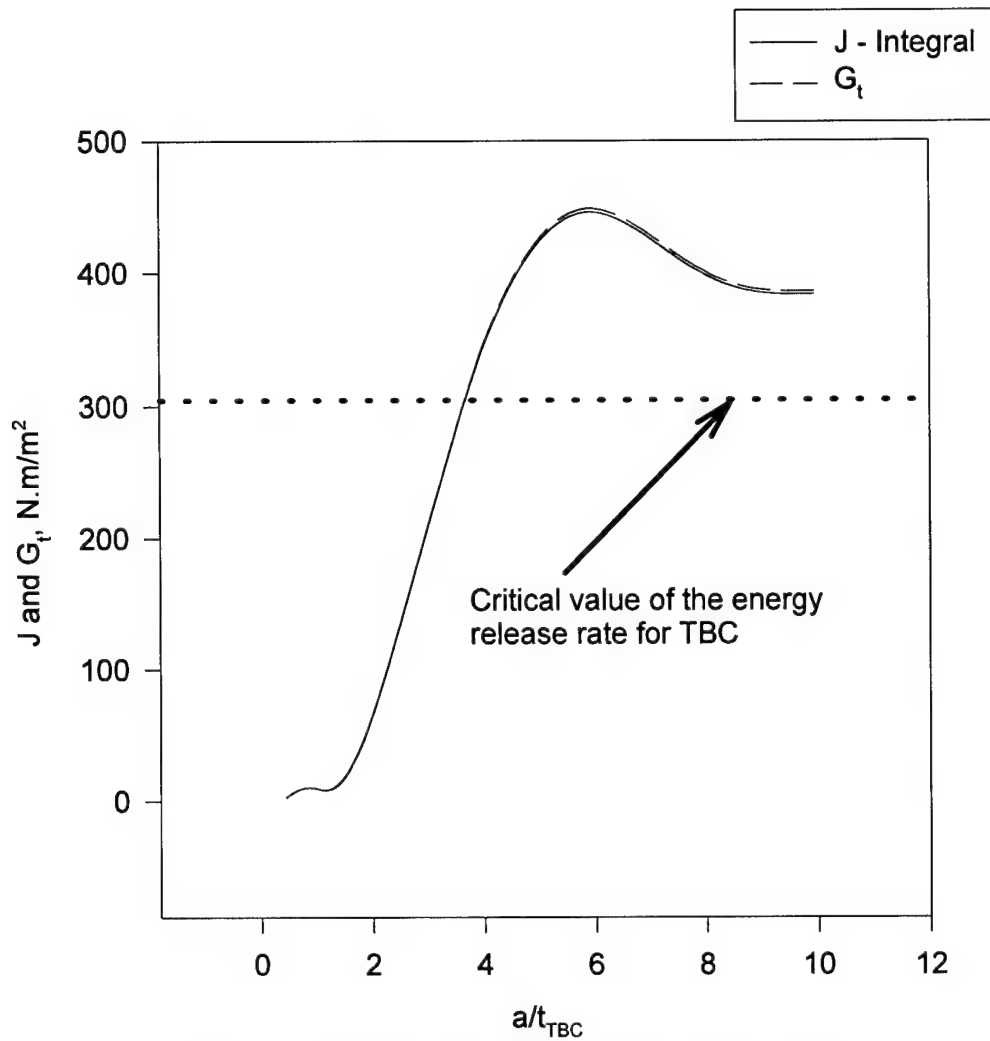


Figure 7. Variation of J and G_I versus crack length ratio for cylindrical specimen

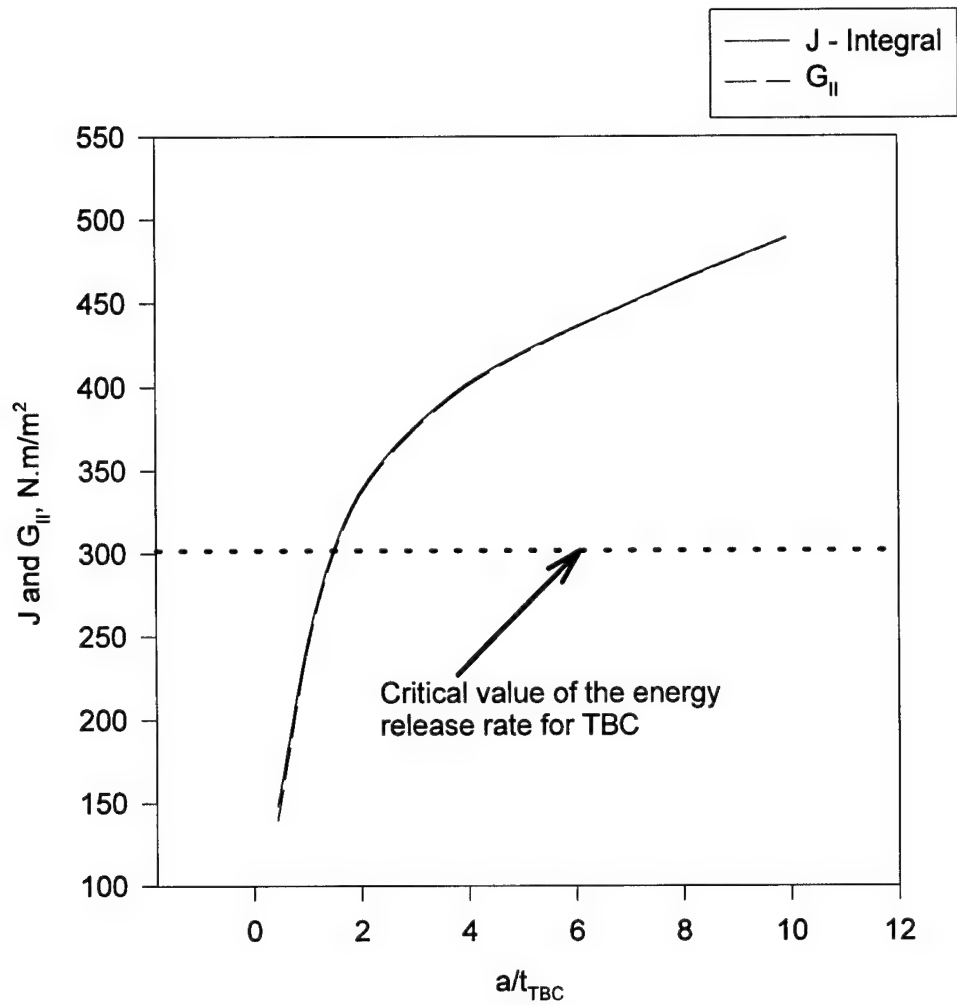


Figure 8. Variation of J and G_{II} versus crack length ratio for stepped-disk specimen

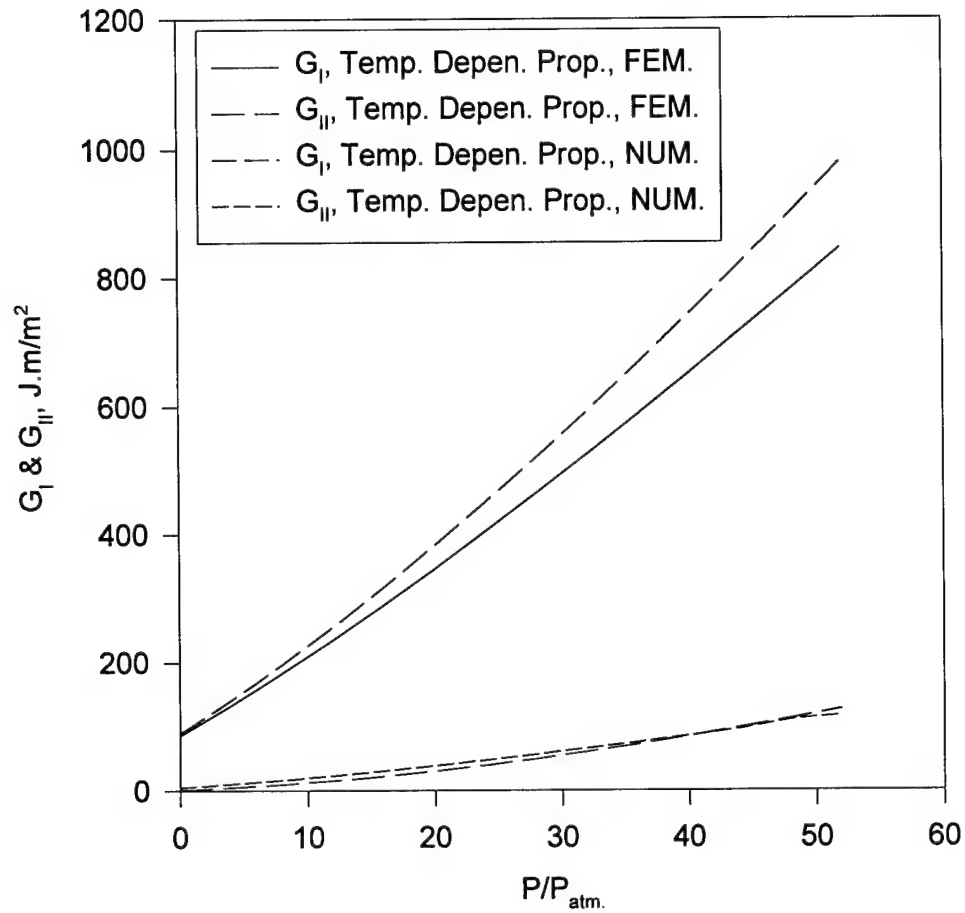


Figure 9. Variation of G_I & G_{II} versus pressure ratio, numerical and finite element method are used, also temperature dependent properties are used in the analysis, $a=20h$.

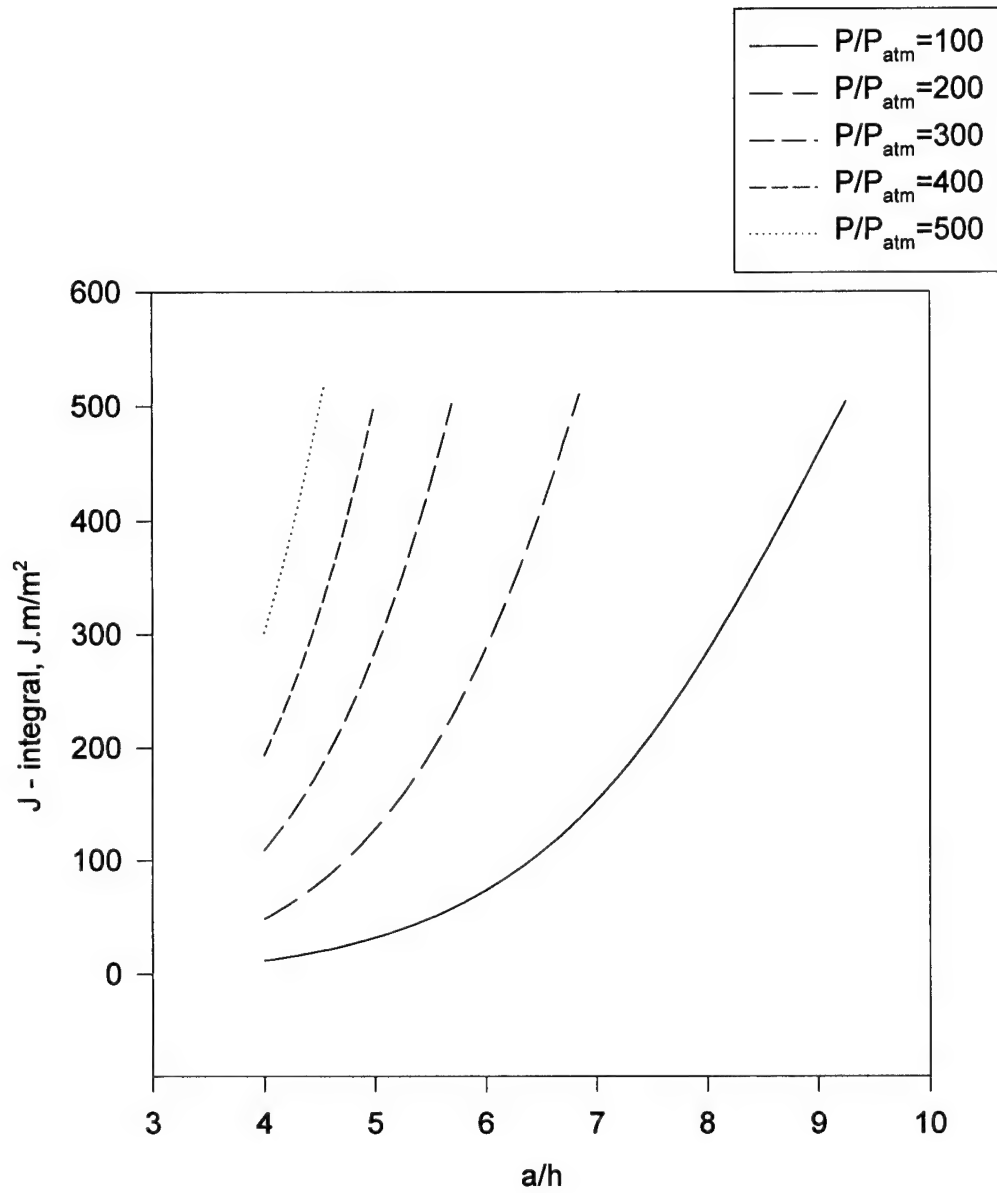
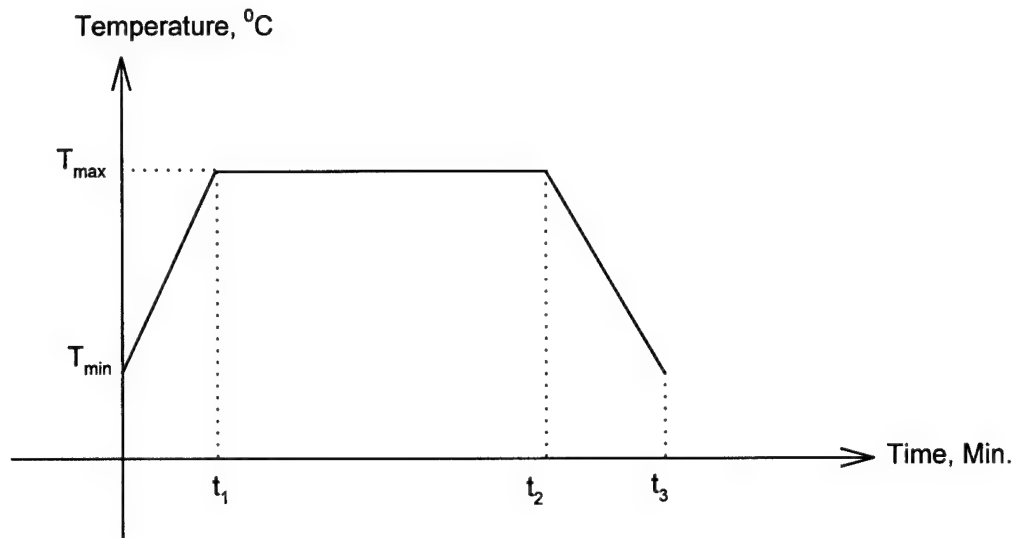


Figure 10. Variation of G versus delamination radius at different pressure ratio, numerical and temperature dependent material properties are used in the analysis.



Cycle	T_{\max}	T_{\min}	t_1	t_2	t_3
A	1177	200	9	54	64
B	1132	200	9	54	64
C	1172	200	9	69	79
D	1172	200	9	609	619

Figure 11. Thermal cycling profiles

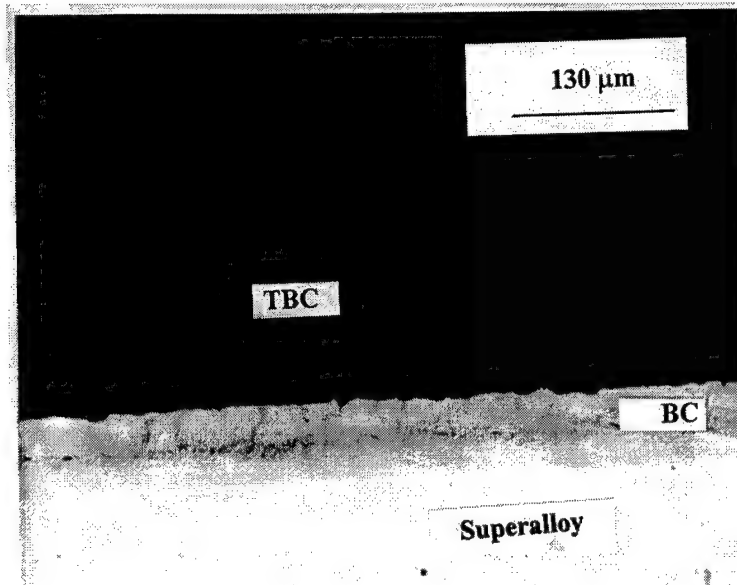


Figure 12 shows an optical micrograph of an untested thermal barrier coated sample. Thermally grown oxide (TGO) layer and/or interfacial separation were absent at the bond coat/top coat (TBC) interface.

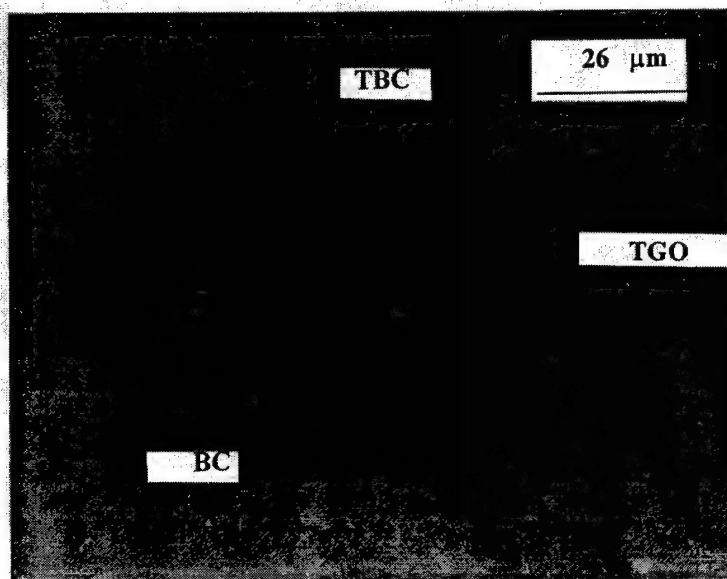


Figure 13 shows an optical micrograph of a tested thermal barrier coated sample. Thermally grown oxide (TGO) layer and/or interfacial separation were seen at the bond coat/top coat (TBC) interface. The sample was thermally cycled to 2 cycle (type A).

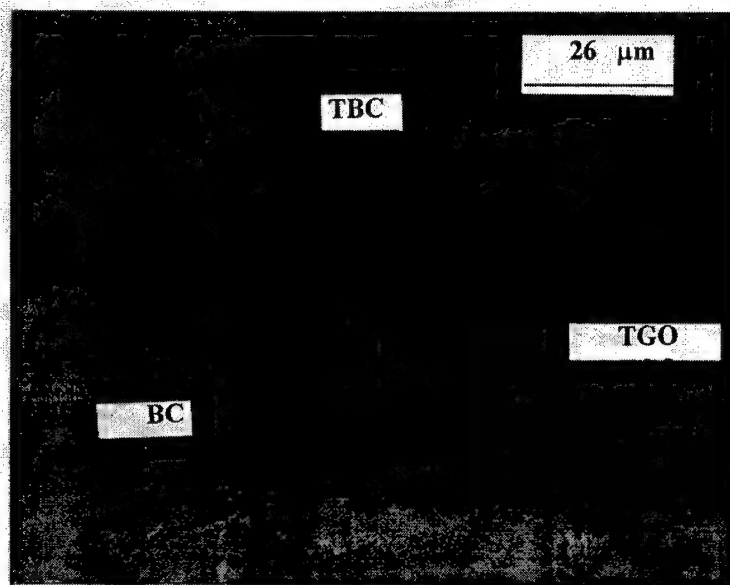


Figure 14 shows an optical micrograph of a tested thermal barrier coated sample. Thermally grown oxide (TGO) layer and/or interfacial separation were seen at the bond coat/top coat (TBC) interface. The sample was thermally cycled to 25 cycle (type A).

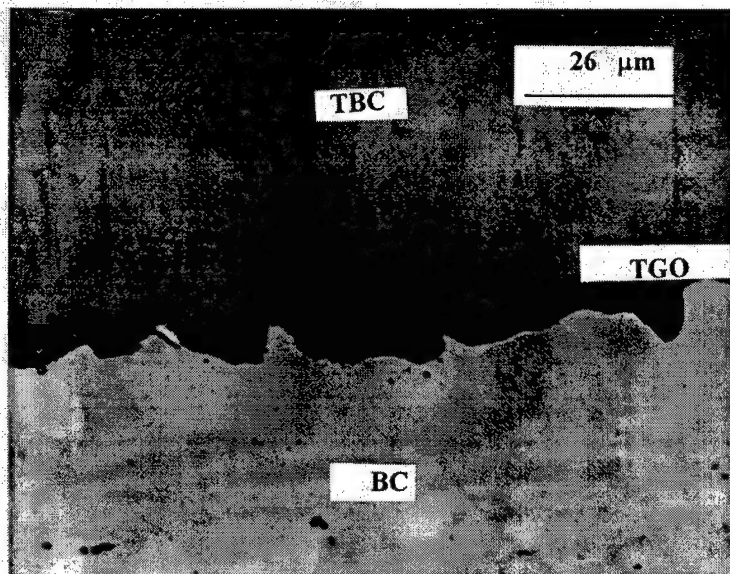


Figure 15 shows an optical micrograph of a tested thermal barrier coated sample. Thermally grown oxide (TGO) layer and/or interfacial separation were seen at the bond coat/top coat (TBC) interface. The sample was thermally cycled to 50 cycle (type A).

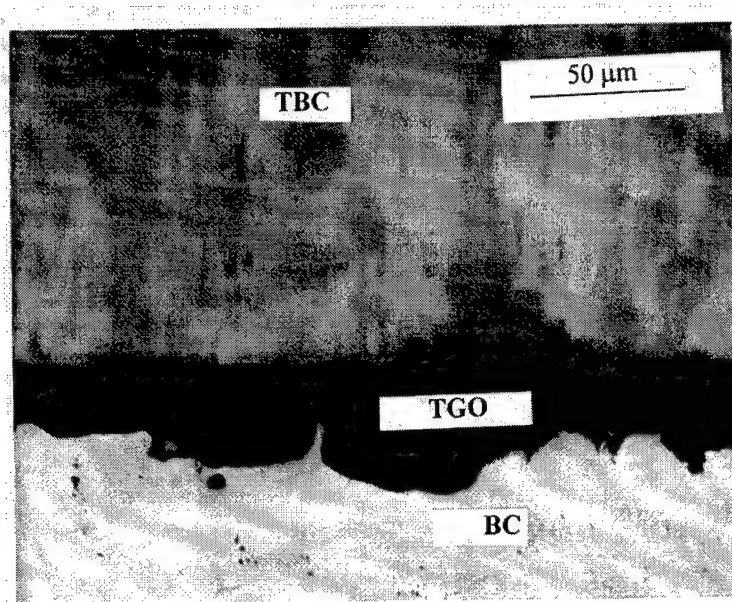


Figure 16 shows an optical micrograph of a tested thermal barrier coated sample. Thermally grown oxide (TGO) layer and/or interfacial separation were seen at the bond coat/top coat (TBC) interface. The sample was thermally cycled to 110 cycle (type A).

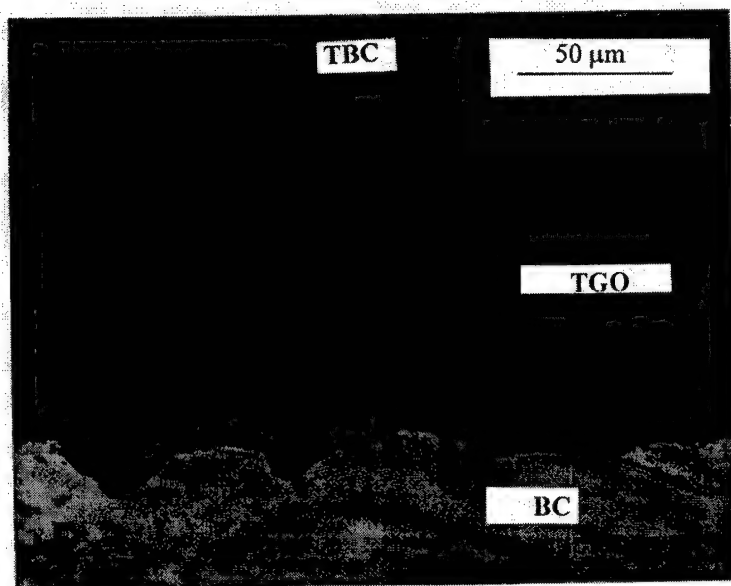


Figure 17 shows a middle optical micrograph of a tested thermal barrier coated sample. Thermally grown oxide (TGO) layer and/or interfacial separation were seen at the bond coat/top coat (TBC) interface. The sample was thermally cycled to 175 cycle (type A).

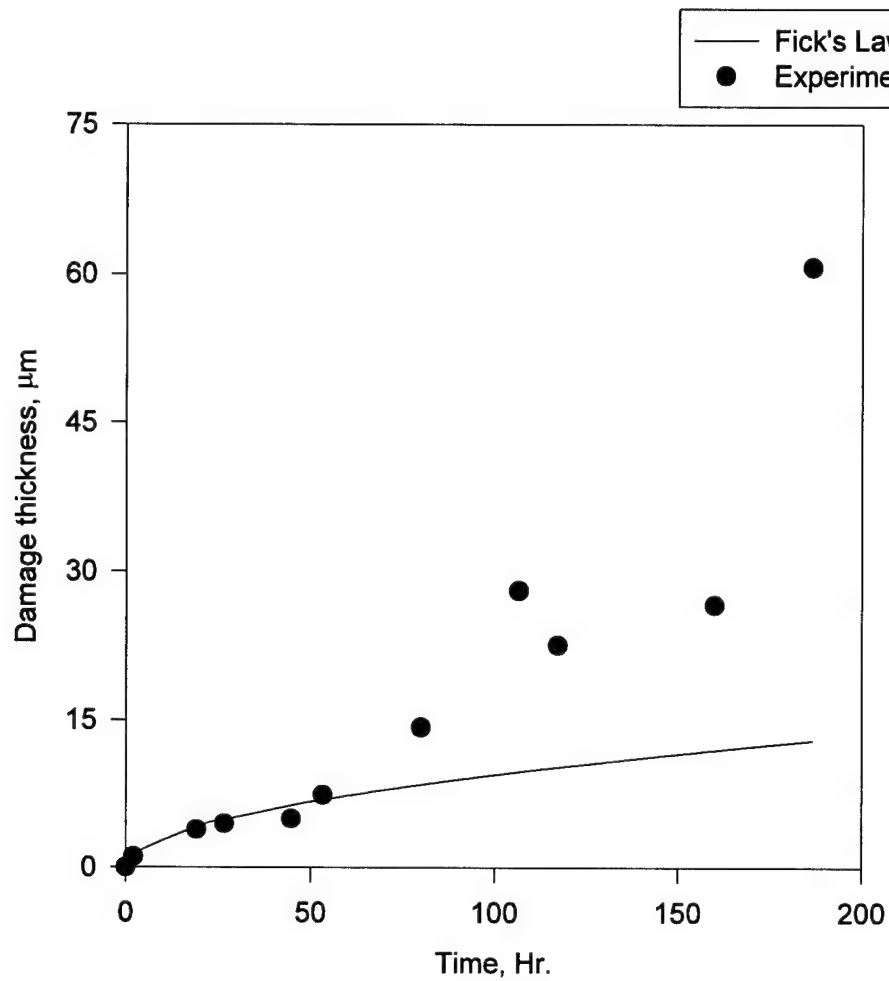


Figure 18. Comparison of experimental data and prediction using Fick's law for TGO buildup as a function of the total cycle time for thermal cycle A.

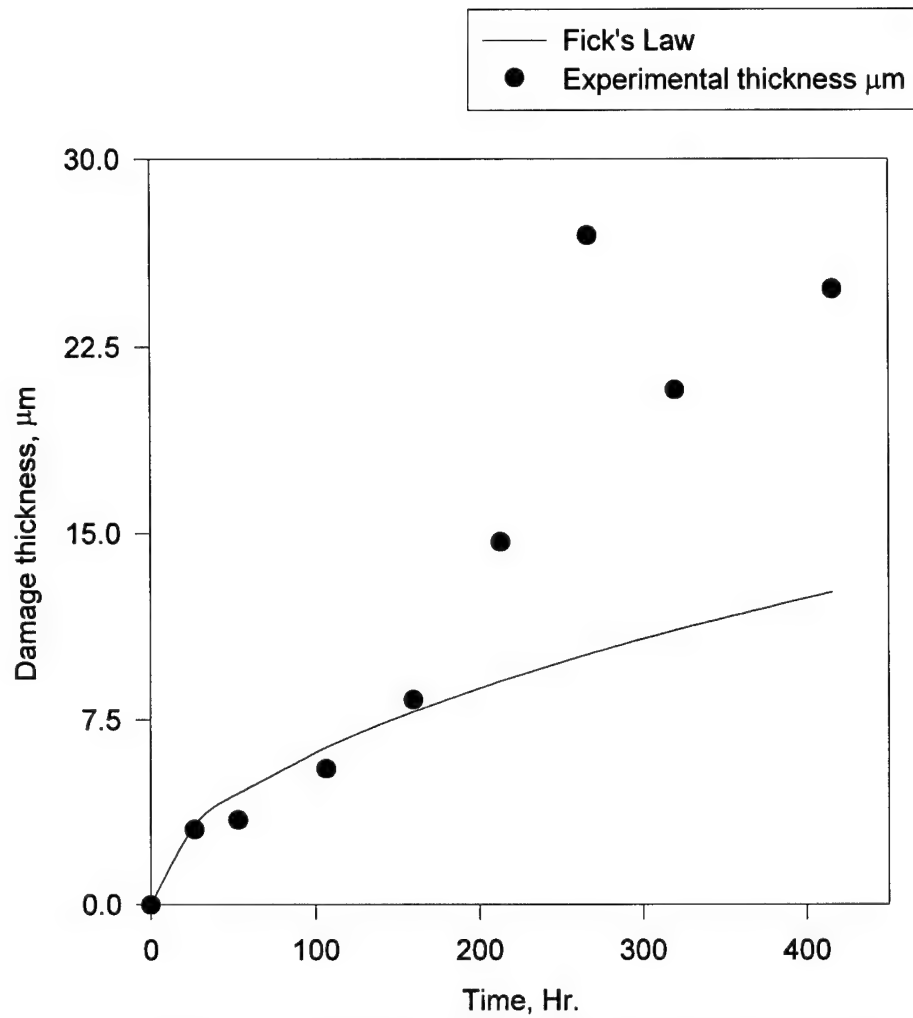


Figure 19. Comparison of experimental data and prediction using Fick's law for TGO buildup as a function of total cycle time for thermal cycle B.

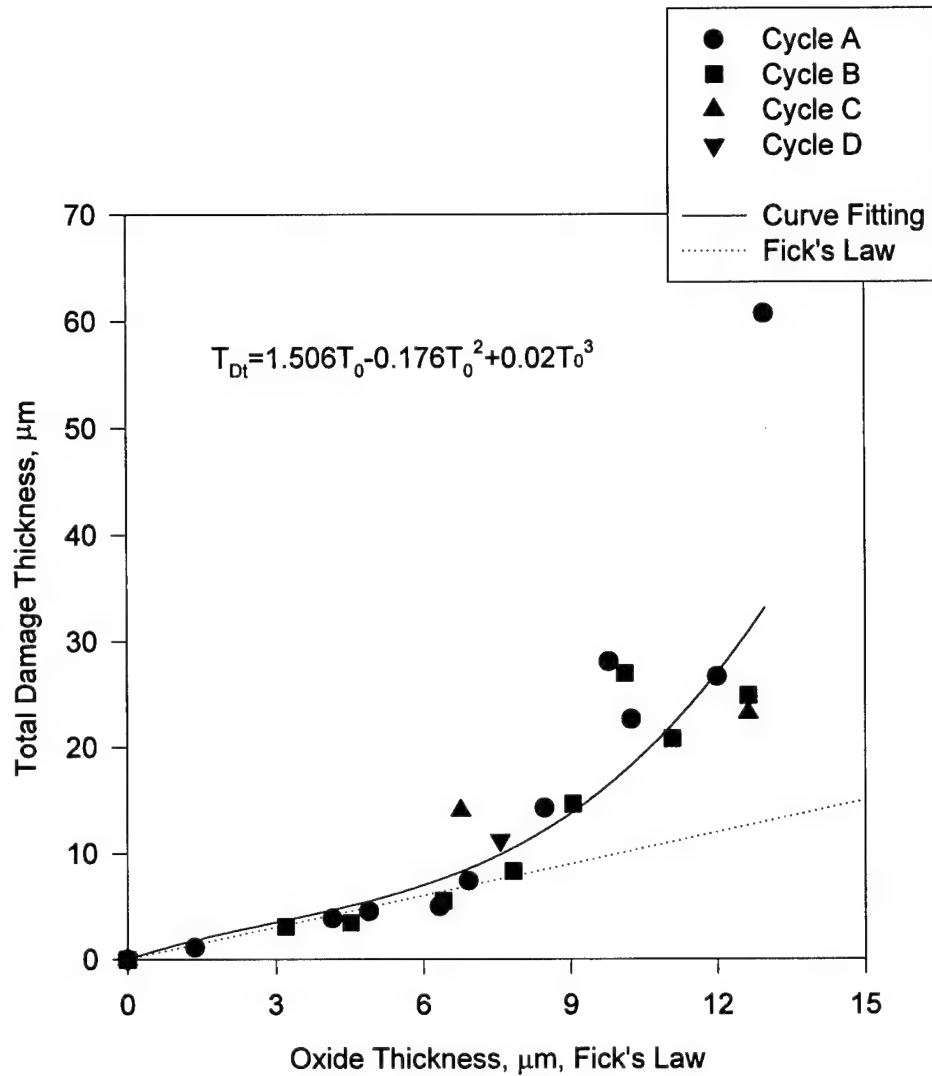


Figure 20. Total damage thickness (experimental output) versus oxide thickness (Fick's law) for different thermal cycling profiles.

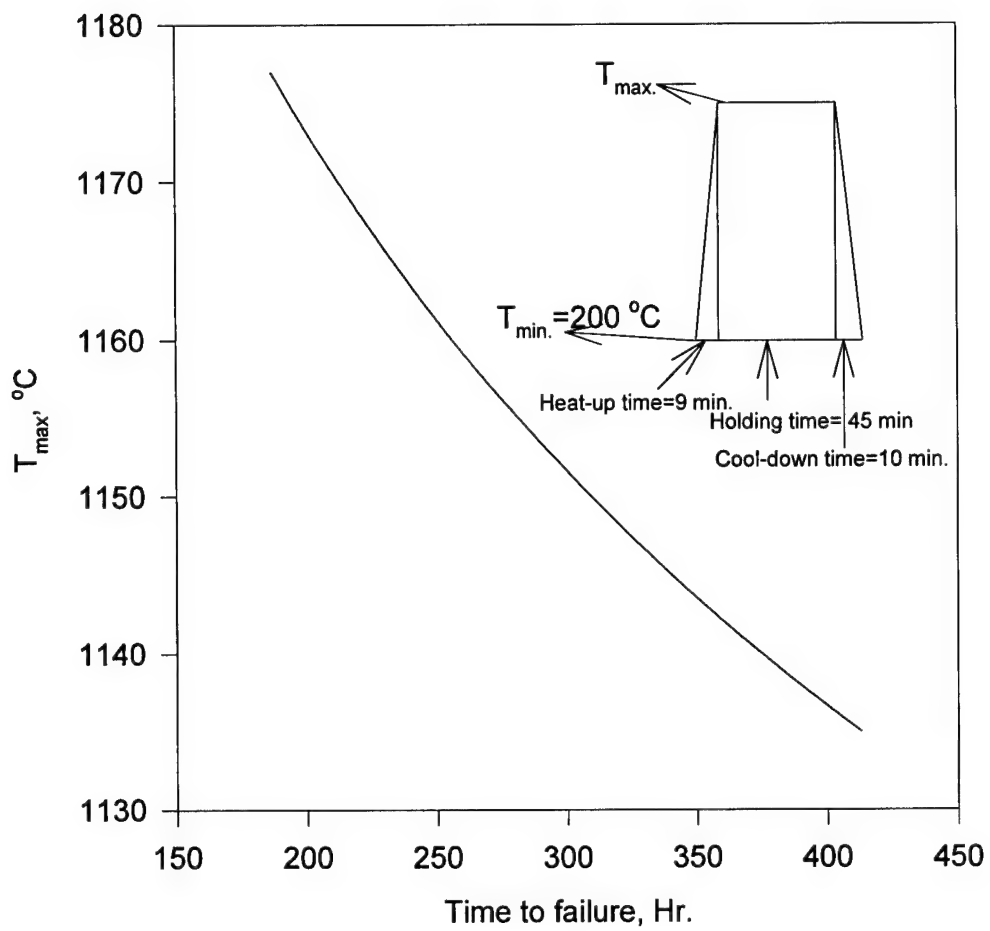


Figure 21. Variation of T_{\max} versus time to failure based on Fick's law and critical oxide thickness ($13\ \mu\text{m}$).

Comparison of thermal wave images at various thermal cycling and corresponding surface temperature profile across the specimens

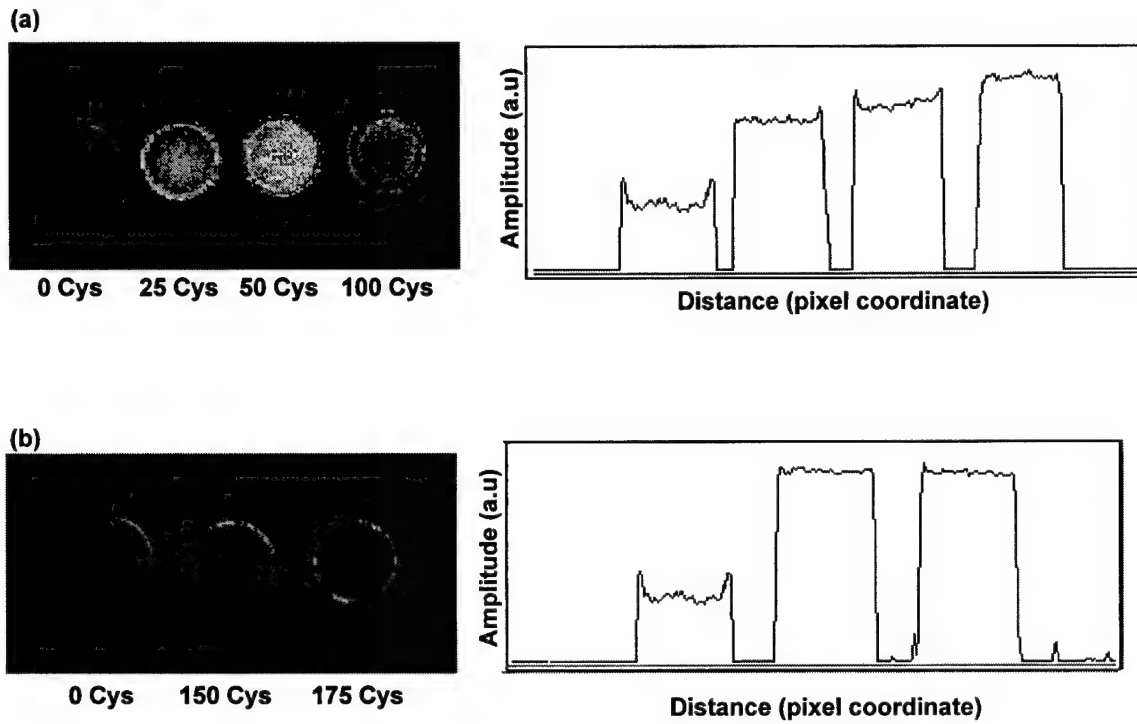


Figure 22. The thermal wave image of six samples at 0, 25, 50, 100, 150 and 175 thermal cycles (cycle type A) and their corresponding surface temperature profiles across the specimens.

APPENDIX

Transient Residual Stresses in Thermal Barrier Coatings: Analytical and Numerical Results

S. Q. Nusier

Assoc. Mem. ASME

G. M. Newaz

Assoc. Mem. ASME

Mechanical Engineering Department,
Wayne State University,
Detroit, MI 48202

Thermal barrier coatings (TBCs) provide thermal insulation to high-temperature superalloys. Residual stresses develop in TBCs during cool-down from processing temperatures due to the thermal expansion mismatch between the different layers (substrate, bond coat, and the ceramic TBC). These residual stresses can initiate microcracks at the bond coat/TBC interface which can lead to debonding at the bond coat/TBC interface. Elasticity-based modeling was used to determine the transient stresses in the TBC, bond coat, and the superalloy substrate with specific attention to the interfaces. For the steady-state case, finite element modeling was undertaken as well. Closed-form elasticity solutions correlated well with the finite element results for the steady-state case. The highest residual stresses occurred at the interface between the bond coat and the TBC. An important result of this investigation was that the TBC/bond coat interface was under biaxial stress field. An important result was that the residual stresses developed in the substrate are higher for the case of partly cooled specimen compared to the fully cooled specimen which can be rationalized due to the presence of higher temperature gradients at earlier times during cool-down from processing temperature.

Introduction

Thermal barrier coatings (TBCs) provide thermal insulation and the bond coat provides oxidation resistance at high temperatures. Ceramic matrix composites (CMCs) can be used for high-temperature application, whereas metallic substrate such as superalloys cannot perform at this high temperature without this ceramic layer, i.e., the TBC. Plasma-sprayed zirconia-yttria ceramic layer with a nickel-chromium-aluminum-yttrium bond coat on a substrate made of nickel-based superalloy (Chang et al., 1987) is a common superalloy/TBC system. Application of these superalloys can be found in aircraft engine (advanced gas turbines) parts such as ducts, vanes, and blades, etc. In automotive applications, the piston head for diesel engine is coated to achieve longer life time and higher performance in terms of fuel reduction and power. However, these coatings have durability problems, due to the material and thermal mismatch between the coating and the metallic substrate. Thermal residual stresses develop during cool down from processing temperatures. These residual stresses may initiate microcracks such as debonding and radial cracks and can have a profound effect on the response of the TBC and interfacial damage accumulation and failure. Their understanding is essential to predict the behavior of the coatings and their performance.

A quantitative determination of the stress states in a model thermal barrier coating as it cools down from the processing temperature (stress-free) to another lower temperature was studied by Chang, et al., (1987). Considering a three-layer concentric cylinder model and a plane-strain condition, they

clearly illustrated the importance of the coefficient of thermal expansion of the bond coat and the Young's modulus of the TBC. The finite element approach was used by these authors. The experimental method and finite element approach was used by Holmes (1988) to study thermal fatigue of coated superalloys of a stepped-disk specimen. The results obtained for the various stress-strain histories clearly illustrate that both the compressive strains encountered on specimen heatup and the tensile strains encountered on cool-down can have a profound effect on useful coating life. An elastic-plastic finite element method was formulated to study residual stresses developed at graded ceramic-metal interfaces during cool-down by Williamson et al., (1993). The results demonstrate the importance of accounting for plasticity when comparing graded and nongraded interfaces. They studied the effects of different interlayer thicknesses and nonlinear composition profiles on strain and stress distributions established during cool down (Drake et al., 1993). Mikata and Taya (1985) studied the stress field in a coated continuous fiber composite subjected to thermomechanical loading, a four-layer concentric circular model was used. The displacement approach was used by Kardomateas (1989) to study the transient thermal stress problem for a hollow circular cylinder. He presented the variation of stresses as function of time and thickness. The effects of circumferential variation of the heat transfer coefficient and gas radiation in three concentric cylinders were studied by Chung et al. (1985). They determined the transient two-dimensional temperature distribution by using the finite element method. Transient thermal stresses in fully and partly cooled circular rings were investigated by Iwaki (1986). He showed that the thermal stress in the fully cooled circular ring is not always greater than that in the partly cooled circular ring. Thermal fracture of multilayer ceramic thermal barrier coatings was studied by Takenchi and Kokini (1994). Controlled experiments along with finite element modeling were used. Their work showed that surface cracks are formed as a result of tensile stresses that are created following stress relaxation in the TBC at steady-state high temperatures. The effect of a transient ther-

Contributed by the Applied Mechanics Division of THE AMERICAN SOCIETY OF MECHANICAL ENGINEERS for publication in the ASME JOURNAL OF APPLIED MECHANICS.

Discussion on the paper should be addressed to the Technical Editor, Professor Lewis T. Wheeler, Department of Mechanical Engineering, University of Houston, Houston, TX 77204-4792, and will be accepted until four months after final publication of the paper itself in the ASME JOURNAL OF APPLIED MECHANICS.

Manuscript received by the ASME Applied Mechanics Division, Oct. 3, 1995; final revision, Aug. 21, 1997. Associate Technical Editor: M. Taya.

mal load on a coating which is bonded to a cylindrical substrate was studied by Kokini and Hornack (1988). The finite element method was used to obtain a solution for a circumferential edge crack normal to the coating. Their analysis showed that smaller heat transfer rates result in smaller stress intensity factors. The initial phase of transient thermal stresses due to general boundary thermal loads in an orthotropic hollow cylinder was studied by Kardomateas (1990). Kardomateas and Chung (1994) studied the case of orthotropic cylindrical shell loaded by an external pressure under imposed constant moisture concentrations on the inner and outer surfaces. They obtained an exact elasticity solution for stresses and displacements. The thermomechanical response of ceramically coated metal parts in elevated thermal environments were investigated by Padovan et al., (1984, 1985). A finite element algorithm was used in their analysis. The thermomechanical oxidation response of thermal barrier coatings was studied by Padovan et al., (1986). They solved the field equations with the associated boundary conditions numerically.

A thermal barrier coated high-temperature substrate in the form of a cylinder is a multilayer system with a number of interfaces. The substrate is first coated with a bond coat whose primary function is to provide oxidation protection and to enhance bonding of the thermal barrier coating (TBC) to the overall system. The TBC layer, the bond coat, and the substrate have different thermal expansion coefficients. As a result due to thermal loading and related excursion, each layer may experience residual thermal stresses. Prior to reaching a steady-state situation, the thermal residual stresses can vary significantly over time, particularly, at early times, say within the first 100 seconds of cooling. Therefore, the problem of transient residual stresses can become quite important and can affect the bond coat/TBC and the substrate/bond coat interfaces. Numerical solution techniques are often utilized for such problems provided that the geometry of the multilayer system is amenable to idealization. However, for TBC systems there no closed-form solutions available to determine the overall temperature field and subsequently to obtain the transient residual stress field. In the current work, a concentric cylinder model is taken for representing a realistic superalloy substrate coated with bond coat and TBC and to obtain an elasticity solution that describes the transient residual stress fields.

In our investigation, the primary focus was to analytically predict the transient thermal residual stress distribution at the various interfaces of the TBC/bond coat/superalloy system and compare the results with finite element stress analysis results. Evaluation of residual stresses is treated until it reaches a steady-state condition. These solutions provide an insight into the influence of thermal and material mismatch stresses at the interfaces in TBC coated superalloy systems, particularly in identifying conditions that lead to interfacial separation due to thermal loads.

Modeling Aspects

For the case of N concentric cylinders, it is possible to get an exact elasticity solution far away from the edges. This provides a better understanding of the type of stresses that exist, and also we will be able to verify these stresses with the finite element solution. The elasticity solution is developed as follows.

Transient Temperature Solution. Consider a one-dimensional multiphase region consisting of N concentric cylinders, where the outermost one is layer number one and the innermost one is solid and has a layer number N . Continuity of temperature and heat flux was assumed to be across the interfaces (perfect thermal contact between the layers at the interfaces). The governing equation for the transient temperature field is

$$\frac{\partial^2 T_i}{\partial r^2} + \frac{1}{r} \frac{\partial T_i}{\partial r} = \frac{1}{\alpha_i} \frac{\partial T_i}{\partial t}$$

$$i = 1, 2, \dots, N \quad r_{i+1} < r < r_i \quad t > 0. \quad (1)$$

The boundary conditions are

$$T_{i+1}(r_{i+1}, t) = T_i(r_{i+1}, t) \quad i = 1, 2, \dots, N-1 \quad t > 0 \quad (2)$$

$$k_{i+1} \frac{\partial T_{i+1}(r_{i+1}, t)}{\partial r} = k_i \frac{\partial T_i(r_{i+1}, t)}{\partial r} \quad i = 1, 2, \dots, N-1 \quad t > 0 \quad (3)$$

$$hT_1(r_1, t) + k_1 \frac{\partial T_1(r_1, t)}{\partial r} = 0 \quad t > 0. \quad (4)$$

The initial condition is

$$T_i(r, 0) = T_0 \quad r_{i+1} < r < r_i \quad i = 1, 2, \dots, N \quad t = 0, \quad (5)$$

where α_i is the thermal diffusivity, k_i is the thermal conductivity, t is the time, and h is the convection heat transfer coefficient. The above boundary value problem of heat conduction is solved by applying the orthogonal-expansion technique over multilayer regions (Ozisik, 1968; Tittle, 1965; Tittle and Robenson, 1965). The temperature function $T(r, t)$ can be represented in an infinite series of a separated space (r) and time (t) variables in the following form:

$$T(r, t) = \sum_{n=1}^{\infty} A_n \cdot X_{jn}(r) \cdot e^{-\alpha_j \omega_{jn}^2 t} \quad j = 1, 2, \dots, N \quad (6)$$

where A_n are arbitrary constants and $X_{jn}(r)$ are the eigenfunctions associated with the above eigenvalue problem. The solution of this eigenvalue problem will have the form

$$X_{jn}(r) = B_{jn}[J_0(\omega_{jn}r) + C_{jn}Y_0(\omega_{jn}r)] \quad r_{i+1} < r < r_i \quad i = 1, 2, \dots, N \quad (7)$$

where J_n and Y_n are Bessel function of the first and second kind, receptively. Since there is no energy storage in the infinitesimal thickness of the interface, the time behavior of the temperature at the interface should be the same on both sides. In mathematical form, this condition is written as

$$\alpha_{j-1} \omega_{(j-1)n}^2 = \alpha_j \omega_{jn}^2 \quad j = N-1, \dots, 1. \quad (8)$$

For the case of uniform initial temperature (T_0) all over the regions, the coefficient A_n is written as

$$A_n = \frac{\sum_{j=1}^N \frac{k_j}{\alpha_j} \int_{r_{j+1}}^{r_j} T_0 \cdot X_{jn}(r) \cdot r \cdot dr}{\sum_{j=1}^N \frac{k_j}{\alpha_j} \int_{r_{j+1}}^{r_j} T_0 \cdot X_{jn}^2(r) \cdot r \cdot dr} \quad (9)$$

By applying the boundary conditions, the coefficients B_{jn} , C_{jn} and the eigenvalues ω_{jn} can be evaluated.

Now, consider the case of the three concentric cylinders. The temperature functions for the layers are

$$T_1(r, t) = \sum_{n=1}^{\infty} A_n \cdot X_{1n}(r) \cdot e^{-\alpha_1 \omega_{1n}^2 t} \quad r_2 < r < r_1 \quad (10)$$

$$T_2(r, t) = \sum_{n=1}^{\infty} A_n \cdot X_{2n}(r) \cdot e^{-\alpha_2 \omega_{2n}^2 t} \quad r_3 < r < r_2 \quad (11)$$

$$T_3(r, t) = \sum_{n=1}^{\infty} A_n \cdot X_{3n}(r) \cdot e^{-\alpha_3 \omega_{3n}^2 t} \quad 0 < r < r_3. \quad (12)$$

The eigenfunctions are

$$X_{1n}(r) = B_{1n}[J_0(\omega_{1n}r) + C_{1n}Y_0(\omega_{1n}r)] \quad r_2 < r < r_1 \quad (13)$$

$$X_{2n}(r) = B_{2n}[J_0(\omega_{2n}r) + C_{2n}Y_0(\omega_{2n}r)] \quad r_3 < r < r_2. \quad (14)$$

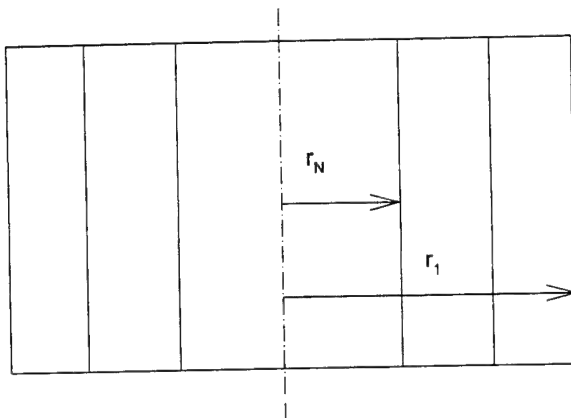


Fig. 1 N-phase concentric cylinder model

$$X_{3n}(r) = J_0(\omega_{3n}r) \quad 0 < r < r_3 \quad (15)$$

The eigenvalues are related by

$$\alpha_1 \omega_{1n}^2 = \alpha_2 \omega_{2n}^2 = \alpha_3 \omega_{3n}^2 \quad (16)$$

By applying the boundary conditions (Eqs. (2), (3), (4)), one can get the following:

$$k_1 \omega_{1n} [J_1(\omega_{1n} r_1) + C_{1n} Y_1(\omega_{1n} r_1)] = h [J_0(\omega_{1n} r_1) + C_{1n} Y_0(\omega_{1n} r_1)] \quad (17)$$

$$J_0(\omega_{3n} r_3) = B_{2n} [J_0(\omega_{2n} r_3) + C_{2n} Y_0(\omega_{2n} r_3)] \quad (18)$$

$$B_{2n} [J_0(\omega_{2n} r_2) + C_{2n} Y_0(\omega_{2n} r_2)] = B_{1n} [J_0(\omega_{1n} r_2) + C_{1n} Y_0(\omega_{1n} r_2)] \quad (19)$$

$$k_3 \omega_{3n} J_1(\omega_{3n} r_3) = k_2 \omega_{2n} B_{2n} [J_1(\omega_{2n} r_3) + C_{2n} Y_1(\omega_{2n} r_3)] \quad (20)$$

$$k_2 \omega_{2n} B_{2n} [J_1(\omega_{2n} r_2) + C_{2n} Y_1(\omega_{2n} r_2)] = k_1 \omega_{1n} B_{1n} [J_1(\omega_{1n} r_2) + C_{1n} Y_1(\omega_{1n} r_2)] \quad (21)$$

Equations (17)–(20) along with Eq. (16) could be solved for the following unknowns, C_{1n} , C_{2n} , B_{1n} , B_{2n} , ω_{1n} , ω_{2n} , ω_{3n} .

The solution for these equations is obtained by eliminating all of the unknowns except ω_{1n} , the final equation is solved for the root ω_{1n} by using the bisection method. Finally, all the other unknowns were evaluated in terms of the known eigenvalue ω_{1n} . The coefficients A_n is evaluated by using Eq. (9) ($j = 3$ for this case). After integration and simplification, A_n is given by

$$A_n = \frac{2T_0}{r_3 \omega_{3n}} \frac{J_1(\omega_{3n} r_3) + \sum_{i=1}^2 \frac{k_{i+1}}{k_3} \left(\frac{\alpha_3}{\alpha_{3-i}} \right)^{0.5} \left[\frac{r_{3-i}}{r_3} Z_1(\omega_{(3-i)n} r_{3-i}) - Z_1(\omega_{(3-i)n} r_{4-i}) \right]}{J_0^2(\omega_{3n} r_3) + J_1^2(\omega_{3n} r_3) + \sum_{i=1}^2 \frac{k_{i+1}}{k_3} \left(\frac{\alpha_3}{\alpha_{3-i}} \right) \sum_{j=0}^1 \frac{r_{3-i-j}^2}{r_3^2} [Z_j^2(\omega_{(3-i)n} r_{3-i}) - Z_j^2(\omega_{(3-i)n} r_{4-i})]} \quad (22)$$

where $Z_p(X_n) = B_n[J_p(X_n) + C_n Y_p(X_n)]$. Finally, by using Eqs. (10)–(12) the temperature field is well defined.

Stress Field in N Concentric Cylinders Subjected to Thermal Loading. Consider the N concentric long circular cylinders shown in Fig. 1. The outermost cylinder radius is r_1 and the innermost cylinder radius is r_N . The entire model is subjected to axisymmetric temperature change $\Delta T(r, t)$. In general, all the

materials are assumed to be transversely isotropic both in stiffness and thermal expansion, where (r, θ) is the transverse plane.

The equilibrium equations in the r , θ , and z directions are given by (Boley and Weiner, 1960; Manson, 1966; Hasselman and Heller, 1980; Timoshenko and Goodier, 1971),

$$\begin{aligned} \frac{\partial \sigma_{rr}}{\partial r} + \frac{1}{r} \frac{\partial \sigma_{r\theta}}{\partial \theta} + \frac{\partial \sigma_{rz}}{\partial z} + \frac{\sigma_{rr} - \sigma_{\theta\theta}}{r} &= 0 \\ \frac{\partial \sigma_{\theta r}}{\partial r} + \frac{1}{r} \frac{\partial \sigma_{\theta\theta}}{\partial \theta} + \frac{\partial \sigma_{\theta z}}{\partial z} + \frac{2\sigma_{r\theta}}{r} &= 0 \\ \frac{\partial \sigma_{zr}}{\partial r} + \frac{1}{r} \frac{\partial \sigma_{z\theta}}{\partial \theta} + \frac{\partial \sigma_{zz}}{\partial z} + \frac{\sigma_{rz}}{r} &= 0. \end{aligned} \quad (23)$$

The stress-strain relations are

$$\begin{aligned} \sigma_{rr} &= C_{11}\epsilon_{rr} + C_{12}\epsilon_{\theta\theta} + C_{13}\epsilon_{zz} - \beta_1 T \\ \sigma_{\theta\theta} &= C_{12}\epsilon_{rr} + C_{11}\epsilon_{\theta\theta} + C_{13}\epsilon_{zz} - \beta_1 T \\ \sigma_{zz} &= C_{13}\epsilon_{rr} + C_{13}\epsilon_{\theta\theta} + C_{33}\epsilon_{zz} - \beta_3 T \\ \sigma_{rz} &= 2C_{44}\epsilon_{rz} \\ \sigma_{\theta z} &= 2C_{44}\epsilon_{\theta z} \\ \sigma_{r\theta} &= (C_{11} - C_{12})\epsilon_{r\theta} \end{aligned} \quad (24)$$

and

$$\begin{aligned} \beta_1 &= (C_{11} + C_{12})\alpha_T + C_{13}\alpha_L \\ \beta_3 &= 2C_{13}\alpha_T + C_{33}\alpha_L \end{aligned} \quad (25)$$

where C_{ij} are elastic constants, and α_T and α_L are the thermal expansion coefficients along the transverse (r) and the longitudinal (z) directions, respectively. The strain-displacement relations are given by

$$\begin{aligned} \epsilon_{rr} &= \frac{\partial u_r}{\partial r}, \quad \epsilon_{\theta\theta} = \frac{1}{r} \frac{\partial u_\theta}{\partial \theta} + \frac{u_r}{r}, \quad \epsilon_{zz} = \frac{\partial u_z}{\partial z}, \\ \epsilon_{rz} &= \frac{1}{2} \left(\frac{\partial u_z}{\partial r} + \frac{\partial u_r}{\partial z} \right) \\ \epsilon_{\theta z} &= \frac{1}{2} \left(\frac{\partial u_\theta}{\partial z} + \frac{1}{r} \frac{\partial u_z}{\partial \theta} \right), \quad \epsilon_{r\theta} = \frac{1}{2} \left(\frac{1}{r} \frac{\partial u_r}{\partial \theta} + \frac{\partial u_\theta}{\partial r} - \frac{u_\theta}{r} \right) \end{aligned} \quad (26)$$

where σ_{ij} , ϵ_{ij} , and u_i are components of stress, strain, and displacement, respectively. Due to the axisymmetry, the displacement field can be expressed as

$$u_r = u(r), \quad u_\theta = 0, \quad u_z = w(z). \quad (27)$$

A substitution of Eq. (27) into Eq. (26) yields to

$$\epsilon_{rr} = \frac{\partial u}{\partial r}, \quad \epsilon_{\theta\theta} = \frac{u}{r}, \quad \epsilon_{zz} = \frac{\partial w}{\partial z}, \quad \epsilon_{rz} = \epsilon_{\theta z} = \epsilon_{r\theta} = 0. \quad (28)$$

Substituting Eq. (28) into Eq. (24) gives

$$\begin{aligned}\sigma_{rr} &= C_{11} \frac{\partial u}{\partial r} + C_{12} \frac{u}{r} + C_{13} \frac{\partial w}{\partial z} - \beta_1 T \\ \sigma_{\theta\theta} &= C_{12} \frac{\partial u}{\partial r} + C_{11} \frac{u}{r} + C_{13} \frac{\partial w}{\partial z} - \beta_1 T \\ \sigma_{zz} &= C_{13} \frac{\partial u}{\partial r} + C_{13} \frac{u}{r} + C_{33} \frac{\partial w}{\partial z} - \beta_3 T \\ \sigma_{rz} &= \sigma_{\theta z} = \sigma_{r\theta} = 0.\end{aligned}\quad (29)$$

Then the governing equations are obtained in terms of displacements from Eqs. (23) and (29)

$$C_{11} \frac{d^2 u}{dr^2} - C_{11} \frac{u}{r^2} + \frac{C_{11}}{r} \frac{du}{dr} = \beta_1 \frac{dT}{dr}, \quad \frac{d^2 w}{dz^2} = 0. \quad (30)$$

Now, for the case of three concentric long circular cylinders, the boundary conditions are given by

$$\begin{aligned}\sigma_{rr}(r_1) &= 0 \\ u_1 &= u_2, w_1 = w_2, \sigma_{rr}^1 = \sigma_{rr}^2 \quad \text{at } r = r_2 \\ u_2 &= u_3, w_2 = w_3, \sigma_{rr}^2 = \sigma_{rr}^3 \quad \text{at } r = r_3 \\ \int_0^{r_3} \sigma_{zz}^3 r dr + \int_{r_3}^{r_2} \sigma_{zz}^2 r dr + \int_{r_2}^{r_1} \sigma_{zz}^1 r dr &= 0.\end{aligned}\quad (31)$$

The general solution to Eq. (30) is given by

$$\begin{aligned}u(r, t) &= Ar + \frac{B}{r} + \frac{r}{2} \int g(r, t) dr - \frac{1}{2r} \int r^2 g(r, t) dr \\ w(z) &= Ez + F\end{aligned}\quad (32)$$

where

$$g(r, t) = \frac{\beta_1}{C_{11}} \frac{dT}{dr}. \quad (33)$$

$F = 0$, and substitution of Eq. (32) into Eq. (29), yields

$$\begin{aligned}\sigma_{rr}^n &= C_{11}^n \left[A_n - \frac{B_n}{r^2} + C_n(r, t) - \frac{D_n(r, t)}{r^2} \right] \\ &+ C_{12}^n \left[A_n + \frac{B_n}{r^2} + C_n(r, t) + \frac{D_n(r, t)}{r^2} \right] \\ &+ C_{13}^n E - \beta_1^n T_n(r, t) \\ \sigma_{\theta\theta}^n &= C_{12}^n \left[A_n - \frac{B_n}{r^2} + C_n(r, t) - \frac{D_n(r, t)}{r^2} \right] \\ &+ C_{11}^n \left[A_n + \frac{B_n}{r^2} + C_n(r, t) + \frac{D_n(r, t)}{r^2} \right] \\ &+ C_{13}^n E - \beta_1^n T_n(r, t) \\ \sigma_{zz}^n &= 2C_{13}^n [A_n + C_n(r, t)] + C_{33}^n E - \beta_3^n T_n(r, t),\end{aligned}\quad (34)$$

where n is referred to as the cylinder under consideration, $n = 1$ is the outermost cylinder, $n = 2$ is the middle cylinder, and $n = 3$ is the innermost cylinder, and where

$$\begin{aligned}C_n(r, t) &= \frac{1}{2} \int g_n(r, t) dr = \frac{\beta_1^n}{2C_{11}^n} T_n(r, t) \\ D_n(r, t) &= \frac{-1}{2} \int r^2 g_n(r, t) dr = \frac{\beta_1^n}{2C_{11}^n} \sum_{m=1}^{\infty} A_m B_{nm} e^{-\alpha_m r} e^{-\omega_m^2 t} \\ &\times [r^2 [J_2(\omega_{nm} r, t) + C_{nm} Y_2(\omega_{nm} r, t)]].\end{aligned}\quad (35)$$

Now, when the materials are isotropic, both in stiffness and in thermal expansion, we have

$$\begin{aligned}C_{11}^1 &= C_{33}^1 = 2\mu_1 + \lambda_1, C_{12}^1 = C_{13}^1 = \lambda_1 \\ C_{11}^2 &= C_{33}^2 = 2\mu_2 + \lambda_2, C_{12}^2 = C_{13}^2 = \lambda_2 \\ C_{11}^3 &= C_{33}^3 = 2\mu_3 + \lambda_3, C_{12}^3 = C_{13}^3 = \lambda_3 \\ \beta_1^1 &= \beta_3^1 = (2\eta_1 + 3\lambda_1)\alpha_1 \\ \beta_1^2 &= \beta_3^2 = (2\eta_2 + 3\lambda_2)\alpha_2 \\ \beta_1^3 &= \beta_3^3 = (2\eta_3 + 3\lambda_3)\alpha_3.\end{aligned}\quad (36)$$

After substituting Eqs. (32), (34), and (36) into the boundary conditions, Eq. (31) yields

$$\begin{aligned}&C_{11}^1 \left[A_1 - \frac{B_1}{r_1^2} + C_1(r_1, t) - \frac{D_1(r_1, t)}{r_1^2} \right] \\ &+ C_{12}^1 \left[A_1 - \frac{B_1}{r_1^2} + C_1(r_1, t) - \frac{D_1(r_1, t)}{r_1^2} \right] \\ &+ C_{13}^1 E - \beta_1^1 T_1(r_1, t) = 0 \\ &A_1 r_2 + \frac{B_1}{r_2} + r_2 C_1(r_2, t) + \frac{D_1(r_2, t)}{r_2} \\ &= A_2 r_2 + \frac{B_2}{r_2} + r_2 C_2(r_2, t) + \frac{D_2(r_2, t)}{r_2} \\ &A_2 r_3 + \frac{B_2}{r_3} + r_3 C_2(r_3, t) + \frac{D_2(r_3, t)}{r_3} \\ &= A_3 r_3 + r_3 C_3(r_3, t) + \frac{D_3(r_3, t)}{r_3} \\ &C_{11}^3 \left[A_3 + C_3(r_3, t) - \frac{D_3(r_3, t)}{r_3^2} \right] \\ &+ C_{12}^3 \left[A_3 + C_3(r_3, t) - \frac{D_3(r_3, t)}{r_3^2} \right] \\ &+ C_{13}^3 E - \beta_1^3 T_3(r_3, t) \\ &= C_{11}^2 \left[A_2 - \frac{B_2}{r_3^2} + C_2(r_3, t) - \frac{D_2(r_3, t)}{r_3^2} \right] \\ &+ C_{12}^2 \left[A_2 - \frac{B_2}{r_3^2} + C_2(r_3, t) - \frac{D_2(r_3, t)}{r_3^2} \right] \\ &+ C_{13}^2 E - \beta_1^2 T_2(r_3, t) \\ &C_{11}^2 \left[A_2 - \frac{B_2}{r_2^2} + C_2(r_2, t) - \frac{D_2(r_2, t)}{r_2^2} \right] \\ &+ C_{12}^2 \left[A_2 - \frac{B_2}{r_2^2} + C_2(r_2, t) - \frac{D_2(r_2, t)}{r_2^2} \right] \\ &+ C_{13}^2 E - \beta_1^2 T_2(r_2, t) \\ &= C_{11}^1 \left[A_1 - \frac{B_1}{r_2^2} + C_1(r_2, t) - \frac{D_1(r_2, t)}{r_2^2} \right] \\ &+ C_{12}^1 \left[A_1 - \frac{B_1}{r_2^2} + C_1(r_2, t) - \frac{D_1(r_2, t)}{r_2^2} \right] \\ &+ C_{13}^1 E - \beta_1^1 T_1(r_2, t)\end{aligned}$$

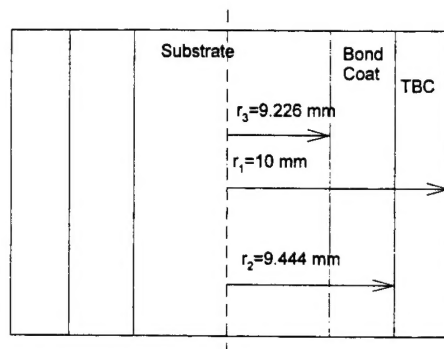


Fig. 2 Dimension of TBC layer in relation to bond coat and superalloy substrate

$$\begin{aligned}
 & (2C_{13}^3 A_3 + C_{33}^3 E) \frac{r_3^2}{2} + (2C_{13}^2 A_2 + C_{33}^2 E) \\
 & \times \frac{r_2^2 - r_3^2}{2} (2C_{13}^1 A_1 + C_{33}^1 E) \frac{r_1^2 - r_2^2}{2} \\
 & + \left(\frac{C_{13}^3 \beta_1^3}{C_{11}^3} - \beta_3^3 \right) \sum_{n=1}^{\infty} A_n B_{3n} e^{-\alpha_3 \omega_{3n}^2 t} \left[\frac{r}{\omega_{3n}} [J_1(\omega_{3n} r, t) \right. \\
 & \left. + C_{3n} Y_1(\omega_{3n} r, t)] \right] \Big|_{r_3}^{\frac{r_3}{2}} \\
 & + \left(\frac{C_{13}^2 \beta_1^2}{C_{11}^2} - \beta_3^2 \right) \sum_{n=1}^{\infty} A_n B_{2n} e^{-\alpha_2 \omega_{2n}^2 t} \left[\frac{r}{\omega_{2n}} [J_1(\omega_{2n} r, t) \right. \\
 & \left. + C_{2n} Y_1(\omega_{2n} r, t)] \right] \Big|_{r_2}^{\frac{r_2}{2}} \\
 & + \left(\frac{C_{13}^1 \beta_1^1}{C_{11}^1} - \beta_3^1 \right) \sum_{n=1}^{\infty} A_n B_{1n} e^{-\alpha_1 \omega_{1n}^2 t} \left[\frac{r}{\omega_{1n}} [J_1(\omega_{1n} r, t) \right. \\
 & \left. + C_{1n} Y_1(\omega_{1n} r, t)] \right] \Big|_{r_1}^{\frac{r_1}{2}} = 0. \quad (37)
 \end{aligned}$$

Equation (37) has six linear equations with six unknowns ($A_1, A_2, A_3, B_1, B_2, E$), and after solving these equations, the stress field is fully defined at every r and t .

Finite Element Stress Analysis

The uncoated nickel-based superalloy specimen had a radius of 9.26 mm, the bond coat layer thickness is 0.184 mm, the TBC thickness is 0.556 mm, and the length of the specimen is 100 mm. These dimensions are shown in Fig. 2. The properties of these three layers are given in Table 1. We analyzed a model

case where the specimen was plasma-sprayed in air with a thin zirconia-yttria (ZrO_2 -8 wt% Y_2O_3) layer on a nickel-chromium-aluminum-zirconium bond coat, as in Chang et al. (1987). The specimen was cooled down from a processing temperature of 1000°C to a temperature of 0°C. A convection heat transfer coefficient (h) of a value 50 W/m²/K was used in the analysis. The finite element model was used for the case of three concentric cylinders using ALGOR for a fully elastic analysis. A quarter model was used since the specimen is axisymmetric and also symmetry is maintained about the middle section. A four-node isoparametric element type was used; the total number of elements was 500. Along the longitudinal axis, the nodes can move in the axial direction only, and along the midsection symmetry line, the nodes can move in the radial direction only.

Results

The orthogonal-expansion technique over a multilayer region was used in order to determine the temperature distribution in the concentric cylinders. The first three roots (ω_{jn}) were found to be dominant in prescribing the temperature field. All other roots are weak and neglected. The axisymmetric condition was applied on the equilibrium equations along with stress-strain relations and strain-displacement relations, so the equilibrium equations reduce to two ordinary differential equations. The transient stress field was obtained by applying the boundary conditions to the solution obtained from those ordinary differential equations. Transient residual stresses have been evaluated for the case of three concentric cylinders by the finite element approach as well as by using the elasticity approach. Figure 3 shows the variation of stress-field components versus time at $r = 2$ mm in the substrate region, it is clear that the stresses are higher for the case of a partly cooled compared to a fully cooled case. Because of the high-temperature gradient in the superalloy, when the time reaches 16.5 seconds, the stresses are maximum. Figure 4 shows the variation of stress-field components versus time at $r = 9.3$ mm in the bond coat region. It is clear that the stresses are higher for the case of a fully cooled compared to that of a partly cooled case. Figure 5 shows the variation of stress-field components versus time at $r = 9.6$ mm in the TBC layer. It is clear that the stresses are higher for the case of a fully cooled compared to a partly cooled case because the temperature field has a high gradient at the earlier stages compared to latest stages. The temperature distribution as a function of time and radial distance is shown in Fig. 6. It is clear that the temperature field has a high gradient at the earlier stages compared to latest stages.

Figure 7 shows the variation of the radial stress versus the radial distance at different times. The peak value occurred close to the center at $t = 16.5$ seconds. Also, Fig. 7 shows that the radial stresses vanish at the outer surface. Radial stresses are not critical for this specimen configuration because of their low values. Note that the radial stress range is 0–25 MPa. Figure

Table 1 Material properties at 22, 566 and 1149°C (Wright, 1995)

Material	Young's modulus (GPa)	Poisson's ratio	Coefficient of thermal expansion (°C ⁻¹)	Coefficient of thermal conductivity (W/m/k)	Coefficient of thermal diffusivity (m ² /s)
Substrate	175.8	0.25	13.91×10^{-6}	7	2×10^{-6}
	150.4	0.2566	15.36×10^{-6}	13	3.4×10^{-6}
	94.1	0.3224	19.52×10^{-6}	22	2.64×10^{-6}
Bond coat	137.9	0.27	15.16×10^{-6}	25	8×10^{-6}
	121.4	0.27	15.37×10^{-6}	50	13.56×10^{-6}
	93.8	0.27	17.48×10^{-6}	65	15.52×10^{-6}
TBC	27.6	0.25	10.01×10^{-6}	1	5×10^{-7}
	6.9	0.25	11.01×10^{-6}	0.96	3.51×10^{-7}
	1.84	0.25	12.41×10^{-6}	1	3.43×10^{-7}

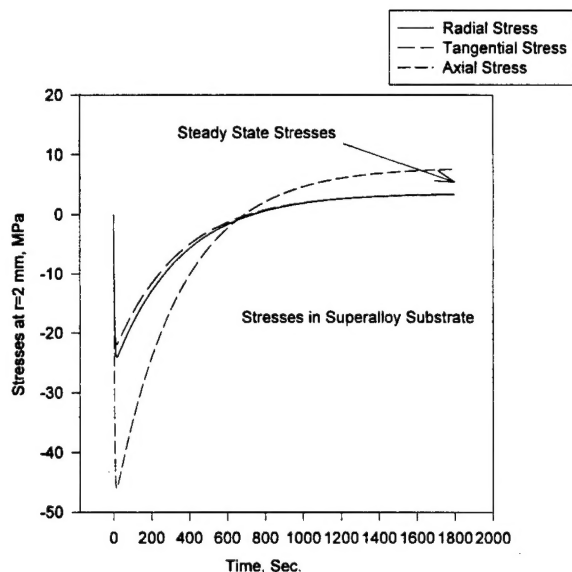


Fig. 3 Variation of stress-field components versus time in the superalloy substrate

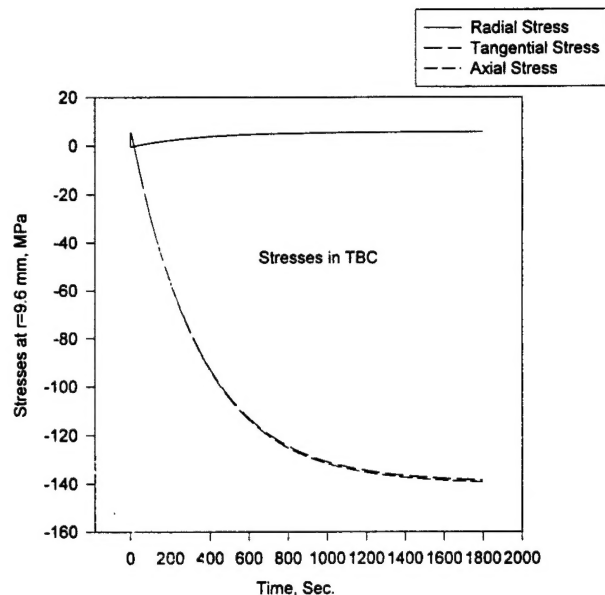


Fig. 5 Variation of stress-field components versus time in the TBC

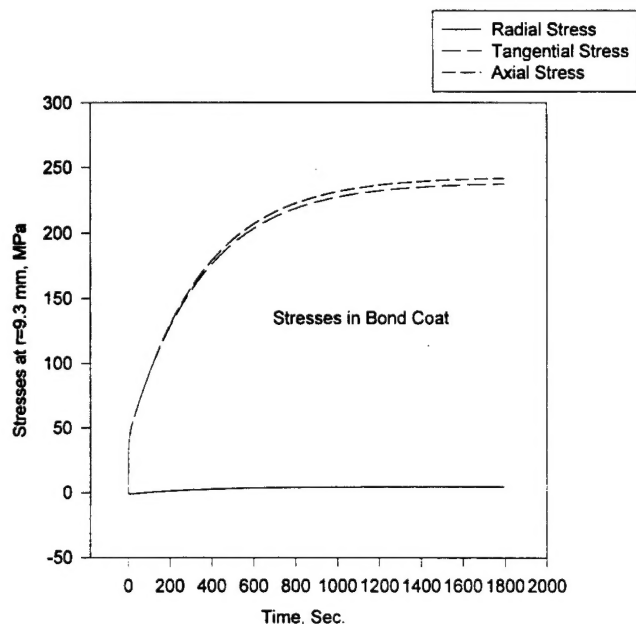


Fig. 4 Variation of stress-field components versus time in the bond coat

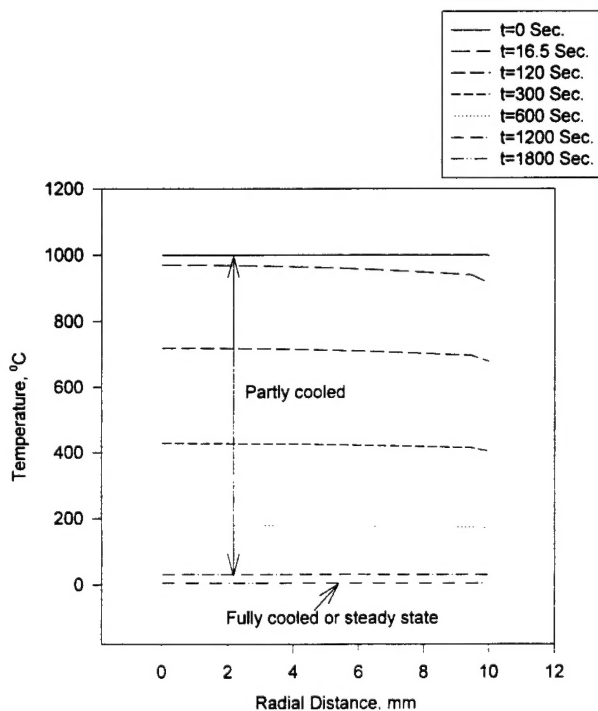


Fig. 6 Temperature versus radial distance at different time for the TBC/bond coat/superalloy system

8 shows the variation of the tangential stress versus the radial distance at different times. From this figure one can see that the maximum stress occurred in the bond coat. Figure 9 shows the variation of the axial stress versus the radial distance at different times, and is the same as in Fig. 8, the maximum axial stress occurred in the bond coat. These figures show excellent agreement between the finite element solution and the elasticity solution for the steady-state case. Bond coat/TBC interface is clearly under the biaxial stress field. The highest tensile stress is 242 MPa and the highest compressive stress is 132 MPa. Figure 10 shows the variation of the axial stress versus the radial distance at different times. In this figure, temperature-dependent properties were used and the results were obtained by using the finite element code ALGOR. By comparing this figure with Fig. 9, it is clear that using temperature-dependent properties, will increase the level of stresses by a factor of 1.7 and the trend will remain same. This effect of using tempera-

ture-dependent properties on the stresses variation for all of the other cases were the same.

Elasticity solution is not valid close to the free edge since the boundary conditions are not satisfied precisely at the free edge. The boundary conditions are subscribed in the average form at any cross section, which may not be precisely valid at the free edge.

Compressive stresses in the TBC play a major role in TBC failure. For example, a flaw size of 12 times the TBC thickness will buckle and spallation of the TBC may occur. The radial stress across the interface generates a driving force which may initiate an interface crack. Subsequently, the interface crack may propagate to failure.

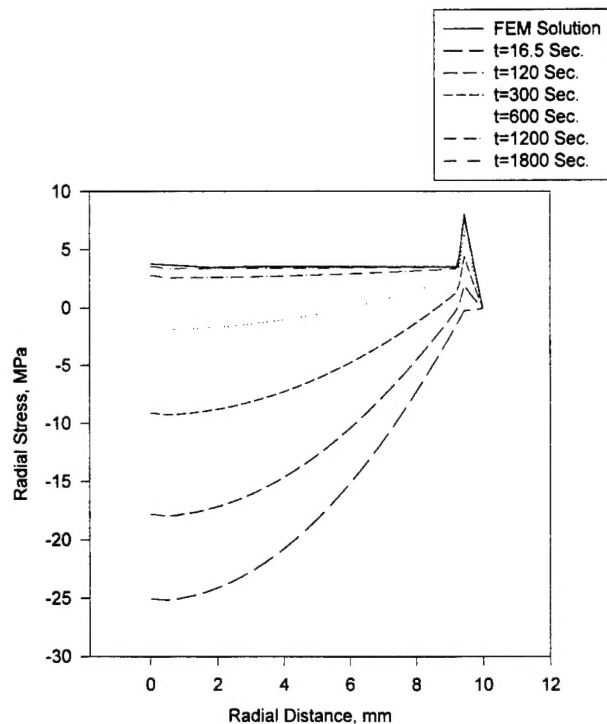


Fig. 7 Radial stress versus radial distance at different times for the TBC/bond coat/superalloy system

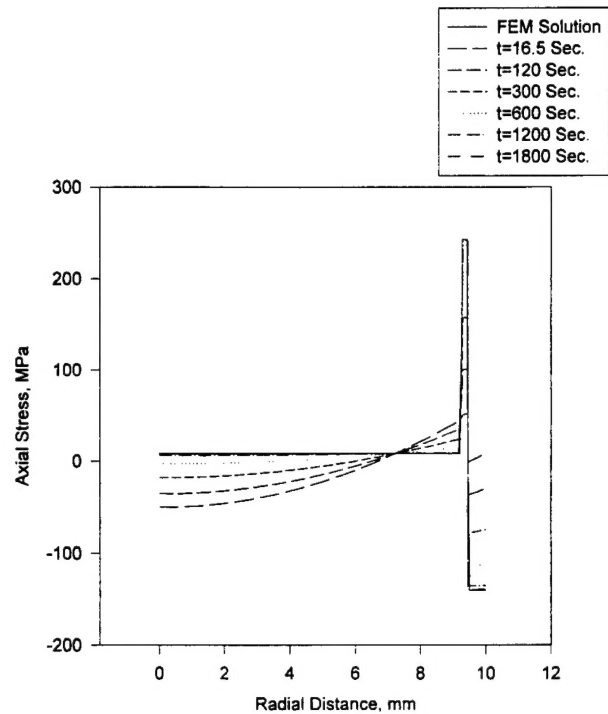


Fig. 9 Axial stress versus radial distance at different time for the TBC/bond coat/superalloy system

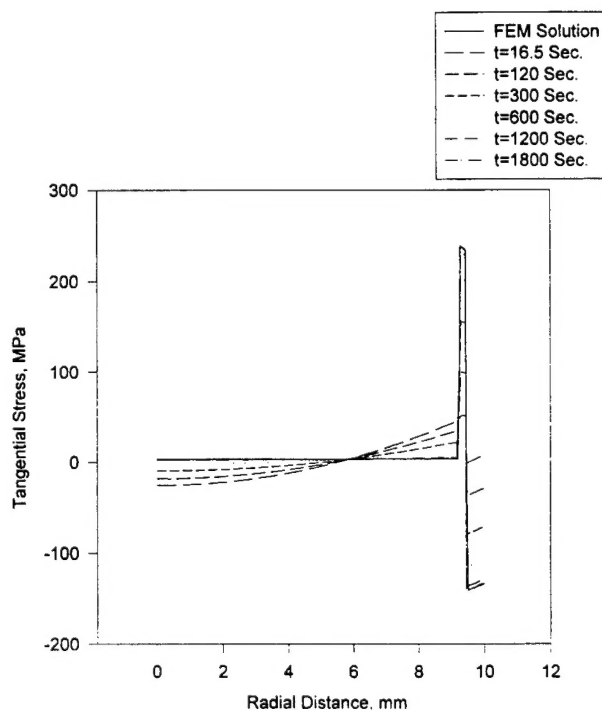


Fig. 8 Tangential stress versus radial distance at different times for the TBC/bond coat/superalloy system

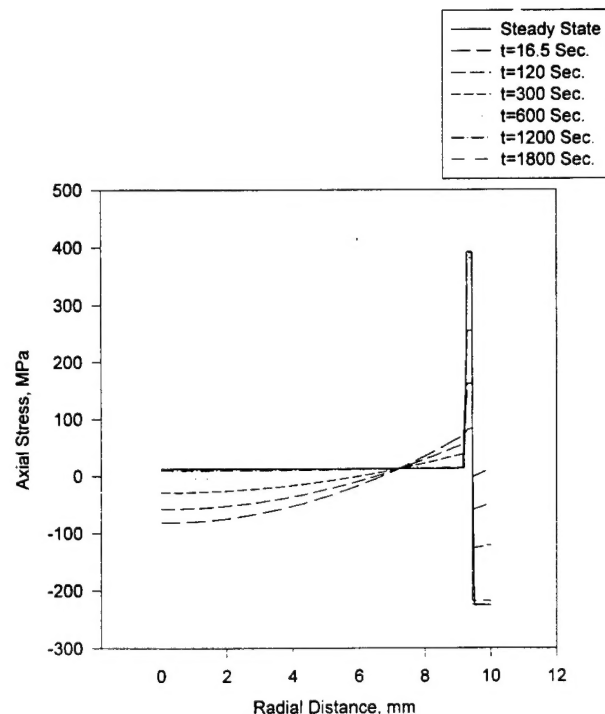


Fig. 10 Axial stress versus radial distance at different times for the TBC/bond coat/superalloy system with temperature-dependent properties

Summary and Conclusions

The orthogonal-expansion technique was utilized over a multilayer region to determine the true temperature field and subsequently to obtain the transient residual stress field. Analysis of the concentric cylinder model representing the TBC/bond coat/superalloy system showed that the elasticity solution and numerical results from finite element stress analyses (steady-

state case only) correlate well in predicting thermal residual stresses in the various layers and at the interfaces. Because of the free-edge condition and stress singularity due to a material mismatch, the elasticity solution is not valid at the free edge of the concentric cylinders. The highest stresses were found to occur at the bond coat/TBC interface. At this interface, results indicate a biaxial stress field due to high axial and tangential

stress; the radial stress component was relatively small. For transient thermal residual analysis, the closed form-elasticity solution can be adequate except at the free edge. The residual stresses developed in the substrate are higher for the case of the partly cooled specimen compared to the fully cooled specimen because the temperature field has a high gradient at the earlier stages compared to later stages.

Acknowledgment

Funding for this research was provided through a grant (# F49620-95-1-0201) from the Air Force Office of Scientific Research (AFOSR). Dr. Walter Jones was the program monitor. Discussion and interaction with Dr. P. K. Wright of GEAE is gratefully acknowledged.

References

- Boley, B. A., and Weiner, J. H., 1960, *Theory of Thermal Stress*, John Wiley and Sons, New York.
- Chang, G. C., and Phucharoen, W., Miller, R. A., 1987, "Finite Element Thermal Stress Solutions for Thermal Barrier Coatings," *Surface and Coatings Technology*, Vol. 32, pp. 307-325.
- Chung, B. T. F., Kermani, M. M., Braun, M. J., Padovan, J., and Hendricks, R. C., 1985, "Heat Transfer in Thermal Barrier Coated Rods with Circumferential and Radial Temperature Gradients," *ASME Journal of Engineering for Gas Turbines and Power*, Vol. 107, pp. 135-141.
- Drake, J. T., Williamson, R. L., and Rabin, B. H., 1993, "Finite Element Analysis of Thermal Residual Stresses at Graded Ceramic-Metal Interfaces. Part II: Interface optimization for residual stress reduction," *J. Appl. Phys.*, Vol. 74, pp. 1321-1326.
- Hasselman, D. P. H., and Heller, R. A., 1980, *Thermal Stresses in Severe Environments*, Plenum Press, New York.
- Holmes, J. W., McClintock, F. A., O'Hara, K. S., and Connors, M. E., 1988, "Thermal Fatigue Testing of Coated Monocrystalline Superalloys," *Low Cycle Fatigue*, ASTM STP 942, pp. 672-691.
- Iwaki, T., 1986, "Transient Thermal Stresses in Fully and Partly Cooled Circular Rings," *Exp. Mech.*, pp. 163-168.
- Kardomateas, G. A., 1989, "Transient Thermal Stresses in Cylindrically Orthotropic Composite Tubes," *ASME JOURNAL OF APPLIED MECHANICS*, Vol. 56, pp. 411-417.
- Kardomateas, G. A., 1990, "The Initial Phase of Transient Thermal Stresses due to General Boundary Thermal Loads in Orthotropic Hollow Cylinders," *ASME JOURNAL OF APPLIED MECHANICS*, Vol. 57, pp. 719-724.
- Kardomateas, G. A., and Chung, C. B., 1994, "Boundary Layer Transient Hygroscopic Stresses in Orthotropic Thick Shells Under External Pressure," *ASME JOURNAL OF APPLIED MECHANICS*, Vol. 61, pp. 161-168.
- Kokini, K., and Hornack, T. R., 1988, "Transient Thermal Load Effects on Coatings Bonded to Cylindrical Substrates and Containing Circumferential Cracks," *ASME Journal of Engineering Materials and Technology*, Vol. 110, pp. 35-40.
- Manson, S. S., 1966, *Thermal Stress and Low-Cycle Fatigue*, McGraw-Hill, New York.
- Mikata, Y., and Taya, M., 1985, "Stress Field in a Coated Continuous Fiber Composite Subjected to Thermo-Mechanical Loadings," *J. of Comp. Mat.*, Vol. 19, pp. 554-578.
- Ozsisik, M. N., 1968, *Boundary Value Problems of Heat Conduction*, Dover, New York.
- Padovan, J., Dougherty, D., Hendricks, B., Bratun, M. J., and Chung, B. T. F., 1984, "High Temperature Thermomechanical Analysis of Ceramic Coatings," *J. of Thermal Stresses*, Vol. 7, pp. 51-74.
- Padovan, J., Dougherty, D., and Hendricks, B., 1986, "Inelastic High-Temperature Thermomechanical Response of Ceramic Coated Gas Turbine Seals," *J. of Thermal Stresses*, Vol. 9, pp. 31-43.
- Padovan, J., Padovan, P., and Xiaru, Y., 1986, "Analysis of Thermomechanical Oxidation Fields in Thermal Barrier Coatings," *J. of Thermal Stresses*, Vol. 9, pp. 251-277.
- Takeuchi, Y. R., and Kokini, K., 1994, "Thermal Fracture of Multilayer Ceramic Thermal Barrier Coatings," *ASME Journal of Engineering for Gas Turbines and Power*, Vol. 116, pp. 266-271.
- Timoshenko, S. P., and Goodier, J. N., 1971, *Theory of Elasticity*, McGraw-Hill, New York.
- Tittle, C. W., 1965, "Boundary-Value Problems in Composite Media: Quasi-Orthogonal Functions," *J. of App. Phys.*, Vol. 36, pp. 1486-1488.
- Tittle, C. W., and Roberson, V. L., 1965, "Analytical Solution of Conduction Problems in Composite Media," *ASME paper 65-WA-HT-52*.
- Williamson, R. L., Rabin, B. H., and Drake, J. T., 1993, "Finite Element Analysis of Thermal Residual Stresses at Graded Ceramic-Metal Interfaces. Part I: Model Description and Geometrical Effects," *J. Appl. Phys.*, Vol. 74, pp. 1310-1320.
- Wright, P. K., 1995, private communication, General Electric Aircraft Engines, Evendale, OH.